X-ray spectroscopy of the unsteady quiescent corona of AD Leo with *Chandra*

A. Maggio[1], J.J. Drake[2], V. Kashyap[2], F.R. Harnden, Jr.[2],
G. Micela[1], G. Peres[3], S. Sciortino[1]

ABSTRACT

We present the analysis and interpretation of an observation of the flare star AD Leo (dM3e) with the Low-Energy Transmission Grating of *Chandra*. The high resolution X-ray spectrum – dominated by emission lines from O VII–VIII, Ne IX–X, and Fe XVII–Fe XIX – allowed us to infer the plasma emission measure distribution (EMD) vs. temperature, and the abundances of individual elements in the corona of this magnetically-active star, during a typical state characterized by significant variability but no evident flaring event. We have also measured plasma densities at various temperatures using spectroscopic diagnostics provided by He-like triplets and Fe XXI lines. We show that the present EMD is similar, in terms of overall shape and temperature of the peak, to those previously obtained from EUVE spectra during quiescent and flaring states confirming the long-term stability of the corona of AD Leo. At variance with the case of other active stars, the EMD of AD Leo is characterized by a significantly shallower slope, compatible with that predicted by static models of isobaric loops with constant cross-section and uniform heating. We discuss such coronal modeling to infer the average properties of the corona in terms of loop populations, including estimates of the surface filling factor derived by comparison between the model and the observed EMD. We also show that the EMD is compatible with the model of a corona continuously heated by flares, which predicts an EMD slope slightly steeper than observed, but that can be accommodated by observational uncertainties. The coronal composition is such that the element abundances, relative to solar values, tend to increase with the First Ionization Potential, with few exceptions. The line to continuum ratios suggest a nearly solar metallicity, a result difficult to reconcile with previous determinations based on global fitting of X-ray spectra.

Subject headings: stars: individual (AD Leo) — stars: activity — stars: coronae — stars: late-type — X-rays: stars

1. Introduction

One of the main challenges of stellar astrophysics today is to infer the characteristics of the magnetic structures that confine hot plasma in stellar coronae and the nature of coronal heating. The topology, surface coverage and strength of the coronal magnetic fields are crucial factors in determining the amount of mass and angular momentum losses via magnetically-coupled stellar winds; such determinations may further our understanding of stellar rotational history, the effects of rotation on stellar evolution and the role normal stars play in the metal enrichment of the interstellar medium and in the chemical evolution of our Galaxy. Determining the plasma temperature and density distributions in stellar coronae, as well as the manner in which these properties change with the X-ray activity level, are key to this understanding.

In this context, active dMe stars are very appealing objects of study because they likely represent the most numerous class of galactic soft X-ray sources, and they allow us to study stellar coronae possibly quite different from the Sun's. In fact, almost all such stars emit X rays in the so-called saturation limit (Pizzolato et al. 2003), having a ratio of X-ray to bolometric luminosity $L_{\rm x}/L_{\rm bol} \approx 10^{-3}$ (compared to $L_{\rm x}/L_{\rm bol} \approx 10^{-6}$ for the Sun), Moreover, the X-ray emission of these stars is highly variable on short time scales (from hundreds of seconds to days) due to the occurrence of many flaring events of different intensities, which might represent one of the main mechanisms for plasma heating (Audard et al. 2000; Kashyap et al. 2002; Güdel et al. 2003), Furthermore, many of these stars are relatively fast rotators compared to the Sun, their convective regions are much deeper and hence their magnetic dynamo activity likely operates on different spatial and temporal scales.

Our present understanding of the corona of AD Leo and a few other dMe stars takes advantage of four different methodologies applied to existing X-ray and EUV data: global spectral fitting of low- or medium-resolution X-ray spectra, analysis of flare decays, time variability studies and plasma emission measure analysis from high-resolution emission line spectra.

X-ray spectra obtained with *ROSAT* and *BeppoSAX* were previously employed to infer the properties of the coronal loop-like structures (Giampapa et al. 1996; Sciortino et al. 1999) by comparison with theoretical models of the magnetically-confined X-ray emitting plasma (Rosner, Tucker, & Vaiana 1978; Serio et al. 1981), in analogy with the case of the solar corona. Such modeling provides estimates of basic parameters like the scale size of the coronal loops, the plasma pressure and the fraction of the stellar surface covered by the emitting regions. In practice, different combinations of these quantities are

[1]INAF – Osservatorio Astronomico di Palermo Giuseppe S. Vaiana, Piazza del Parlamento 1, I–90134 Palermo, Italy; maggio@astropa.unipa.it, micela@astropa.unipa.it, sciorti@astropa.unipa.it.

[2]Smithsonian Astrophysical Observatory, 60 Garden Str., 02138 Cambridge MA, USA; jdrake@cfa.harvard.edu, vkashyap@cfa.harvard.edu, frh@cfa.harvard.edu.

[3]Dipartimento di Scienze Fisiche ed Astronomiche – Sezione di Astronomia – Università di Palermo, Piazza del Parlamento 1, I–90134 Palermo, Italy; peres@astropa.unipa.it.

usually allowed by the data, due to a fundamental degeneracy of the solutions of the models when the structures are smaller than the pressure scale height (Maggio & Peres 1996).

More robust constraints on the sizes of *individual* coronal loops have been derived from a detailed analysis of the decay phase of prominent flaring events, often displayed by active red dwarfs (Reale & Micela 1998; Favata et al. 2000b; Güdel et al. 2004); extrapolation of the results of this analysis to the entire corona relies on the assumptions that the flaring loops are "typical" coronal structures and that the maximum temperature of the plasma in the same structures during quiescent phases can be guessed by fitting low- or medium-resolution X-ray spectra (taken before or after the flares) with simple models that contain a few isothermal components. In fact, the knowledge of the loop size (derived from the flare decay) and of the plasma maximum temperature and total emission measure (derived from the spectral fitting) permits computation of the other relevant parameters (e.g., plasma pressure, surface filling factor) as explained in Sciortino et al. (1999).

Complementary information on the nature of stellar coronae is provided by variability analysis of X-ray or EUV light curves. In particular, the coronal emission of red dwarf stars has been studied by Ambruster, Sciortino, & Golub (1987) using *Einstein* data, by Collura, Pasquini, Schmitt (1988) with EXOSAT, by Giampapa et al. (1996) with ROSAT, and more recently by Kashyap et al. (2002) with EUVE observations. The main result of these studies is that significant variability is continuously observed, and likely associated with flaring events spanning a large range of possible intensities (i.e., released energy); these events might explain the steady presence of hot plasma in the coronae of active stars, by contributing a significant fraction of the total coronal heating.

In this paper we analyze and interpret an observation of the dMe flare star AD Leo obtained with the Low-Energy Transmission Grating Spectrometer (LETGS, Brinkman et al. 2001) on board the *Chandra* X-ray Observatory (Weisskopf et al. 2002). AD Leo has been observed by virtually all previous space-borne X-ray observatories, but the observation discussed here provided the first high-resolution X-ray line spectra from which several diagnostics on the temperature and density structure of the coronal plasma and its chemical abundances can be self-consistently derived. The new information provided by this *Chandra* observation has allowed us to test and improve our understanding of the corona of AD Leo, and to delineate a comprehensive reference scenario for future analyses of the coronal emission of other active M-type dwarfs.

In Sect. 2 we introduce our target and its previous observations, and in Sect. 3 our data reduction approach. Sect. 4 is devoted to the results of our analysis, with most of the technical details relegated to the Appendix. We discuss these results in Sect. 5 and draw our conclusions in Sect. 6.

2. Previous observations of AD Leo

AD Leo is one of the brightest X-ray coronal sources among the *single* dMe stars

Table 1
Target characteristics

Target Name	Parallax (mas)	Spectral Type	$M_{\rm bol}$	Metallicity [Z/H]	Mass $M_\odot$	Radius (cm)
AD Leo (GJ 388)	213 ± 4	M3.5V	8.85	-0.75 ± 0.25	0.40	2.6×10^{10}

References.—Parallax by Jenkins (1952); metallicity by Jones et al. (1996); other parameters by Favata et al. (2000a)

currently known. It is a nearby star (D = 4.7 pc), with an intervening interstellar hydrogen column density $N_{\rm H} = (3 \pm 1) \times 10^{18}\,{\rm cm}^{-2}$, determined from previous observations in the EUV band (Cully et al. 1997). Other characteristics of this object are reported in Table 1, and further discussion of its fundamental parameters (mass $M = 0.4 M_\odot$, radius $R \sim 0.37 R_\odot$, bolometric luminosity $L_{\rm bol} = 8.7 \times 10^{31}$ erg s^{-1}) can be found in Favata et al. (2000a).

Several variability analyses of the coronal emission of AD Leo were performed in the past (see Sect. 1 for a brief review). Most recently, (Favata, Micela, & Reale 2000a) presented an extensive study of X-ray flares on AD Leo, whose results will be discussed in Sect. 5.2, while Sanz Forcada & Micela (2002) and Güdel et al. (2003) have analyzed several EUVE observations.

The quiescent X-ray luminosity of AD Leo was found by Favata et al. (2000a) to be quite stable at $L_{\rm x} = 3$–5×10^{28} erg s^{-1} (0.5–4.5 keV band), in earlier X-ray observations with *Einstein*, *ROSAT*, and *ASCA* that covered a period of 17 yr (1980–1997). On shorter time scales, however, AD Leo is strongly variable: from data taken with the Deep Survey monitor on EUVE, Audard et al. (2000) have estimated a frequency of 7 flares per day with total released energy $E \gtrsim 5 \times 10^{31}$ erg, and 1 flare per day with $E \gtrsim 5 \times 10^{32}$ erg, all above a quiescent EUV luminosity of $\sim 9 \times 10^{28}$ erg s^{-1}.

An attempt has been made by Güdel et al. (2003) to predict the time-averaged plasma emission measure distribution (EMD) vs. temperature in the corona of AD Leo, based on the assumption that the corona is heated by a population of flares with a power-law energy distribution: the results of this exercise appear encouraging but have not yet met the test of an EMD derived from a high signal-to-noise, high-resolution emission line spectra.

Prior to the X-ray analysis presented here, spectra with resolution adequate for a detailed emission measure analysis had been provided by a number of EUVE observations discussed by Cully et al. (1997) and by Sanz Forcada & Micela (2002). These analyses, based essentially on iron lines alone, suggested a complex coronal structure with several possible classes of

TABLE 2
OBSERVATION CHARACTERISTICS

Chandra configuration	ObsId	Start Time	Stop Time	Livetime (s)
LETG + HRC-S	24	2000 Jan 22 20:22:42	2000 Jan 22 23:37:30	9147
LETG + HRC-S	975	2000 Oct 24 15:06:16	2000 Oct 25 04:48:37	48105

coronal loops present at any time. Available line ratio diagnostics indicated the presence of very high density plasma ($N_{\mathrm{e}} \sim$ 5–8 $\times$ $10^{12}\,\mathrm{cm}^{-3}$) at temperatures of 10 MK, even when evident flaring episodes were removed from the data stream.

3. *Chandra* Observations and Reduction

AD Leo was observed twice as part of the *Chandra* GTO program. A first, relatively short observation was followed by a second much longer observation made nine months after the first, as summarized in Table 2. Preliminary results of the analysis of each observation have been presented by Maggio et al. (2001, 2002). Due to the low signal-to-noise (S/N) ratio of the data in the first observation, the present work is based primarily on the 2000 October observation. This observation was recently considered by van den Besselaar et al. (2003), who performed a partial analysis of two separate data segments with the aim of determining the physical conditions of the corona of AD Leo in different states. Their analysis suggests primarily that only the high-temperature tail of the EMD was enhanced during the first segment, but the lack of statistical uncertainties on the EMD values prevents to assess the significance of such enhancement. Since some variation in the amount of hot ($T > 10^7$ k) plasma is an inherent and expected characteristic of such an active star, we feel that a more thorough analysis of the entire second observation is not only justified but also demanded to fully exploit the highest S/N ratio achievable with the available data.

We have re-processed the data with the *Chandra* Interactive Analysis of Observations (CIAO V2.2) software and relevant science threads[4]. In order to optimize the S/N ratio of the target spectrum, this software includes position-dependent PHA filtering of the data (which reduces the background level by a factor $\sim$ 4) and extraction of the (raw) source spectrum from an optimized bow-shaped region, ensuring that a nearly uniform fraction (90% to 94%) of source photons, is collected at all wavelengths. The background spectrum is obtained as the sum of two spectra extracted from symmetrical regions above and below the source region, with each having a uniform area five times that of

[4]http://asc.harvard.edu/ciao/threads

the source area, at all wavelengths.

We computed our net spectrum by subtracting a background spectrum – smoothed with a boxcar filter four pixels wide and scaled to the source region extraction width – from the source spectrum, and then co-adding the positive and negative orders.

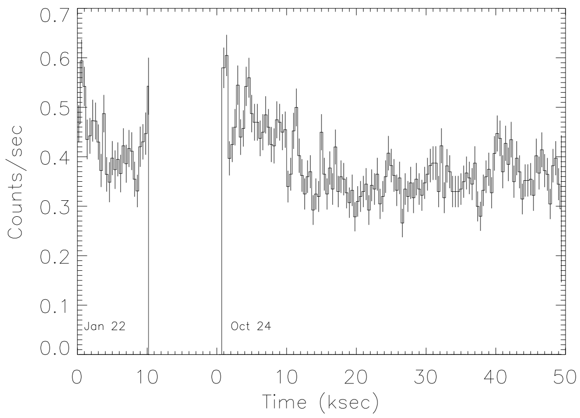

Fig. 1.— AD Leo X-ray light curve (net count rate) extracted from the 0-th order source region. Although no major flare occurred significant variability is present at the 99% statistical confidence level. Bin size is 400 sec, except for the ∼9-month gap (Jan 22 to Oct 24) between the two observations.

4. Analysis and Results

4.1. X-ray light curve

Figure 1 shows the X-ray light curve obtained using the 0th-order source photon arrival times, after subtraction of background collected in an annulus adjacent to the 0th-order source extraction region. No strong isolated flare is visible during the observation, but some low-level variability is clearly present: as quantified by a simple χ^2 test, the light curve deviates from the observed mean count rate (0.38 cnt s^{-1}) at the 99% confidence level. The light curve shows a slowly declining X-ray emission level during the first 12 ksec of the Oct 2000 observation, but we are unable to distinguish whether this is the final decay phase of a flare or some other modulation effect; in fact, the likelihood of a flare is very high, given their observed rate of occurrence (Sect. 2), but a rotational modulation effect cannot be completely excluded because the duration of the October observation is a sizeable fraction (∼ 20%) of the photometric rotational period ($P_{\rm rot}$ = 2.7 d, Spiesman & Hawley 1986). In any case, such variability is typical of the "unsteady corona" of AD Leo, and given the absence of any large variation of the emission level, we have chosen to analyze the spectral data accumulated over the entire length of both observations in order to maximize S/N ratio. A more detailed study of the variability of AD Leo and other active stars observed by *Chandra* will be presented in a forthcoming paper (Argiroffi et al. 2003, in preparation).

4.2. Spectral analysis

The spectral analysis was performed using the software Package for INTeractive Analysis of Line Emission (PINTofALE, Kashyap & Drake 1998) with an iterative procedure including the following steps:

1. Lines were identified on the basis of the CHIANTI V4.02 (Dere et al. 2001) database and a model spectrum synthesized from a trial EMD and trial solar element abundances (Grevesse, Noels, & Sauval 1992), with line emissivities computed by

adopting the ionization balance of Mazzotta et al. (1998). Identifications were subsequently verified with the final EMD and estimated abundances.

2. Line profiles were fit with an analytical approximation to the instrumental line spread function (Sect. A.1) plus a piece-wise constant base level (required to model the source continuum, which was found to be nearly flat. After the first iteration of the analysis, the continuum was adjusted where required to match that predicted by the computed EMD, and the line fitting was repeated if necessary, an important step to ensure the self-consistency of the final result.

3. An emission measure analysis was performed and element abundances (relative to iron) were determined, using both line-by-line inverse emissivity curves and the Markov-Chain Monte Carlo method of Kashyap & Drake (1998), as described in more detail in Sect. A.2.

4. Iron abundance was derived by comparison of the observed continuum with predictions obtained by assuming Fe/H ratios different from the solar ratio.

5. Temperature and density diagnostics were inferred from He-like ion line ratios, based both on the CHIANTI line emissivities and on theoretical calculations by Porquet, Mewe, & Dubau (2001) and taking into account the final EMD. Density diagnostics using sensitive Fe XXI line ratios were also investigated.

Each step of our analysis required considerable care to ensure self-consistency and robustness of the results and to understand the limits of our spectroscopic approach. In the following we describe our most pertinent findings; further details are provided in the Appendix.

The observed spectrum, with identifications of the emitting ion for the most prominent features, is shown in Fig. 2. In total, 120 lines have been identified, including some lines from the overlapping 3rd order spectrum, as reported in Table 3. Iron lines from ionization stages XVI through XXIV have been clearly detected, as well as lines from C, N, O, the other most abundant α elements (Ne, Mg, Si, S, Ni), and one Al line. Overall, the range of temperatures probed by the observed lines extends from $T \sim 10^{5.8}$ K (with the Ne VIII lines) to $T \sim 10^{7.5}$ K (with the Si XIV, Fe XXIII, and Fe XXIV lines).

After a careful examination of the identified lines, we have selected 50 of them for the emission measure analysis, giving preference to lines that have high S/N ratios, are not affected by blending and are not density dependent (see Sect. A.2). Noteworthy among the discarded lines is the Ne X Lyα doublet ($\lambda 12.12, 12.13$ Å), blended with an Fe XVII line that provides about 5% of the measured total flux: according to the final EMD and element abundances this spectral feature appears to be suppressed, in the sense that the measured Ne X Lyα/Lyβ and Lyα/Lyγ ratios are a factor $\gtrsim 2$ lower than expected. This result cannot be attributed to an underestimated contribution from the

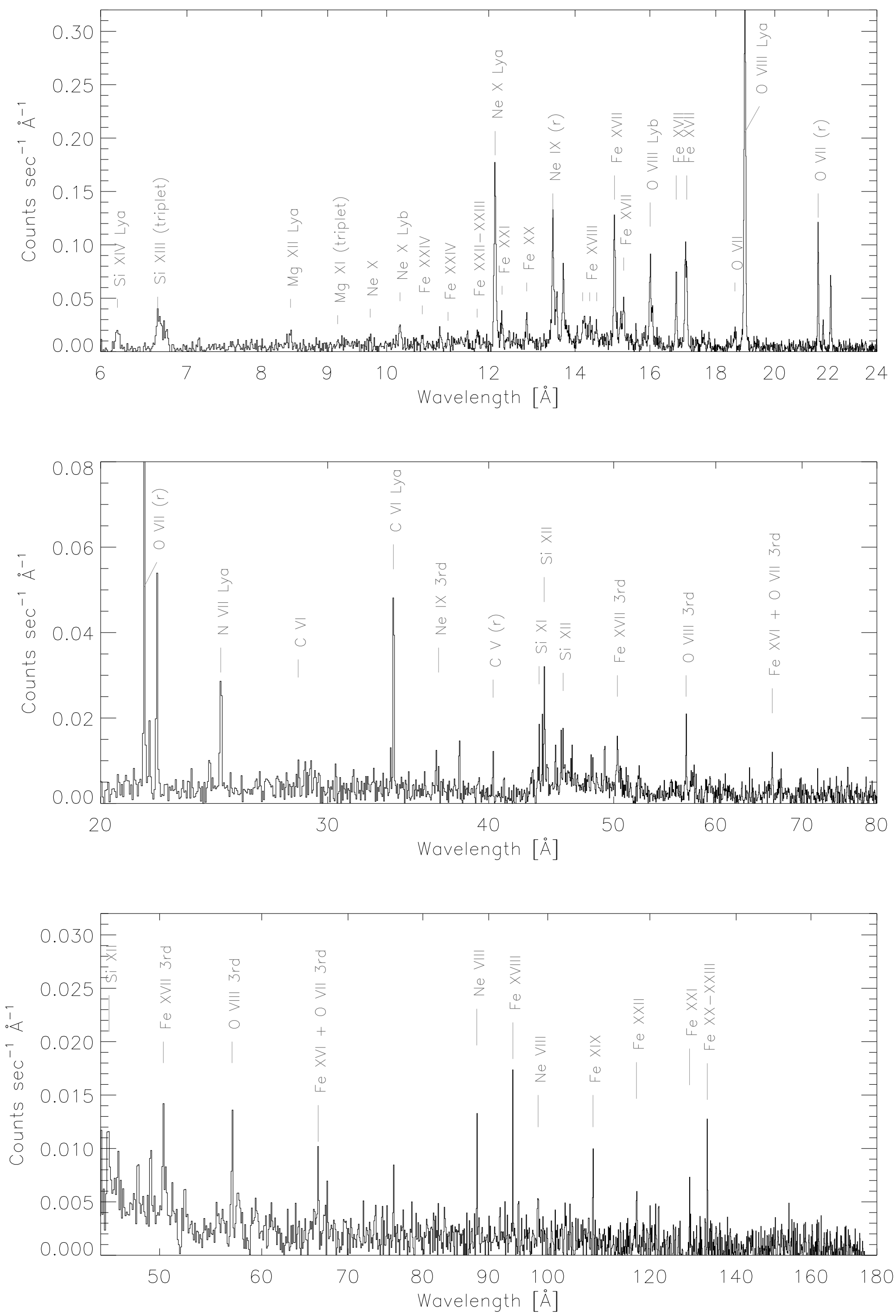

Fig. 2.— AD Leo spectrum, shown in three overlapping wavelength ranges, with line identifications (for the strongest lines) based on the CHIANTI line list. Different Y-axis ranges have been used in the three panels. The bin size is 0.0125 Å in the first wavelength range, while a rebinning by factors 4 and 8 has been performed in the second and third range, respectively. Note that the X-axis scale is logarithmic.

Table 3: Line identifications and fluxes in the AD Leo spectrum.

Label[a]	$\lambda^b_{\rm obs}$	$\lambda^b_{\rm pred}$	Ion	Transition (*upper* → *lower*)	$\log T^c_{\rm max}$	$(F \pm \sigma)^d$	EM^e
1a	6.18	6.18	Si XIV	$2p\ ^2P_{3/2} \rightarrow 1s\ ^2S_{1/2}$	7.20	50 ± 11	Y
1b	···	6.19	Si XIV	$2p\ ^2P_{1/2} \rightarrow 1s\ ^2S_{1/2}$	7.20	···	
2	6.64	6.65	Si XIII	$1s\ 2p\ ^1P_1 \rightarrow 1s^2\ ^1S_0$	7.00	69 ± 14	Y
3a	6.68	6.69	Si XIII	$1s\ 2p\ ^3P_2 \rightarrow 1s^2\ ^1S_0$	6.95	48 ± 13	
3b	···	6.69	Si XIII	$1s\ 2p\ ^3P_1 \rightarrow 1s^2\ ^1S_0$	6.95	···	
4a	6.72	6.72	Si XII	$1s\ 2s\ (^3P)\ 2p\ ^2P_{3/2} \rightarrow 1s^2\ 2s\ ^2S_{1/2}$	6.95	19 ± 11	
4b	···	6.72	Si XII	$1s\ 2s\ (^3P)\ 2p\ ^2P_{1/2} \rightarrow 1s^2\ 2s\ ^2S_{1/2}$	6.95	···	
5	6.75	6.74	Si XIII	$1s\ 2s\ ^3S_1 \rightarrow 1s^2\ ^1S_0$	7.00	32 ± 11	
6a	7.15	7.17	Al XIII	$2p\ ^2P_{3/2} \rightarrow 1s\ ^2S_{1/2}$	7.10	14 ± 8	
6b	···	7.18	Al XIII	$2p\ ^2P_{1/2} \rightarrow 1s\ ^2S_{1/2}$	7.10	···	
7a	8.42	8.42	Mg XII	$2p\ ^2P_{3/2} \rightarrow 1s\ ^2S_{1/2}$	7.00	37 ± 10	Y
7b	···	8.42	Mg XII	$2p\ ^2P_{1/2} \rightarrow 1s\ ^2S_{1/2}$	7.00	···	
8	8.83	8.81	Fe XXIII	$2s\ 4d\ ^1D_2 \rightarrow 2s\ 2p\ ^1P_1$	7.20	15 ± 8	
9	9.16	9.17	Mg XI	$1s\ 2p\ ^1P_1 \rightarrow 1s^2\ ^1S_0$	6.80	22 ± 9	Y
10a	9.23	9.23	Mg XI	$1s\ 2p\ ^3P_2 \rightarrow 1s^2\ ^1S_0$	6.80	15 ± 8	
10b	···	9.23	Mg XI	$1s\ 2p\ ^3P_1 \rightarrow 1s^2\ ^1S_0$	6.80	···	
11	9.31	9.31	Mg XI	$1s\ 2s\ ^3S_1 \rightarrow 1s^2\ ^1S_0$	6.80	24 ± 9	
12a	9.71	9.71	Ne X	$4p\ ^2P_{3/2} \rightarrow 1s\ ^2S_{1/2}$	6.80	25 ± 9	Y
12b	···	9.71	Ne X	$4p\ ^2P_{1/2} \rightarrow 1s\ ^2S_{1/2}$	6.80	···	
13a	10.24	10.24	Ne X	$3p\ ^2P_{3/2} \rightarrow 1s\ ^2S_{1/2}$	6.80	66 ± 12	Y
13b	···	10.24	Ne X	$3p\ ^2P_{1/2} \rightarrow 1s\ ^2S_{1/2}$	6.80	···	
14a	10.66	10.62	Fe XXIV	$1s^2\ 3p\ ^2P_{3/2} \rightarrow 1s^2\ 2s\ ^2S_{1/2}$	7.30	32 ± 10	Y
14b	···	10.66	Fe XXIV	$1s^2\ 3p\ ^2P_{1/2} \rightarrow 1s^2\ 2s\ ^2S_{1/2}$	7.30	···	
15a	11.00	10.98	Fe XXIII	$2s\ 3p\ ^1P_1 \rightarrow 2s^2\ ^1S_0$	7.20	33 ± 10	
15b	···	11.00	Ne IX	$1s\ 4p\ ^1P_1 \rightarrow 1s^2\ ^1S_0$	6.60	···	
16a	11.03	11.02	Fe XXIII	$2s\ 3p\ ^3P_1 \rightarrow 2s^2\ ^1S_0$	7.20	12 ± 9	
16b	···	11.02	Fe XVII	$2s\ 2p^6\ 4p\ ^1P_1 \rightarrow 2p^6\ ^1S_0$	6.80	···	
16c	···	11.03	Fe XXIV	$1s^2\ 3d\ ^2D_{3/2} \rightarrow 1s^2\ 2p\ ^2P_{1/2}$	7.30	···	
17	11.16	11.17	Fe XXIV	$1s^2\ 3d\ ^2D_{5/2} \rightarrow 1s^2\ 2p\ ^2P_{3/2}$	7.30	33 ± 10	Y
18	11.24	11.26	Fe XXIV	$1s^2\ 3s\ ^2S_{1/2} \rightarrow 1s^2\ 2p\ ^2P_{1/2}$	7.30	11 ± 8	Y
19a	11.42	11.43	Fe XXIV	$1s^2\ 3s\ ^2S_{1/2} \rightarrow 1s^2\ 2p\ ^2P_{3/2}$	7.30	36 ± 10	
19b	···	11.44	Fe XXIII	$2s\ 3d\ ^3D_3 \rightarrow 2s\ 2p\ ^3P_2$	7.15	···	
19c	···	11.44	Fe XXII	$2s\ 2p\ (^3P)\ 3p\ ^4S_{3/2} \rightarrow 2s^2\ 2p\ ^2P_{1/2}$	7.10	···	
20	11.54	11.55	Ne IX	$1s\ 3p\ ^1P_1 \rightarrow 1s^2\ ^1S_0$	6.60	38 ± 10	Y
21	11.75	11.74	Fe XXIII	$2s\ 3d\ ^1D_2 \rightarrow 2s\ 2p\ ^1P_1$	7.20	38 ± 11	Y
22	11.79	11.77	Fe XXII	$2s^2\ (^1S)\ 3d\ ^2D_{3/2} \rightarrow 2s^2\ 2p\ ^2P_{1/2}$	7.10	18 ± 10	Y
23a	12.14	12.12	Fe XVII	$2p^5\ 4d\ ^1P_1 \rightarrow 2p^6\ ^1S_0$	6.80	436 ± 24	Y
23b	···	12.13	Ne X	$2p\ ^2P_{3/2} \rightarrow 1s\ ^2S_{1/2}$	6.80	···	
23c	···	12.14	Ne X	$2p\ ^2P_{1/2} \rightarrow 1s\ ^2S_{1/2}$	6.80	···	
24	12.26	12.26	Fe XVII	$2p^5\ 4d\ ^3D_1 \rightarrow 2p^6\ ^1S_0$	6.80	16 ± 11	

Table 3. Continued

$Label^a$	$\lambda^b_{\rm obs}$	$\lambda^b_{\rm pred}$	Ion	Transition (*upper* → *lower*)	$\log T^c_{\rm max}$	$(F \pm \sigma)^d$	EM^e
25	12.29	12.28	Fe XXI	$2s^2\ 2p\ 3d\ ^3D_1 \rightarrow 2s^2\ 2p^2\ ^3P_0$	7.00	67 ± 13	Y
26	12.38	12.38	Fe XXI	$2s^2\ 2p\ 3d\ ^3D_3 \rightarrow 2s^2\ 2p^2\ ^3P_2$	7.00	14 ± 9	
27a	12.41	12.40	Fe XXI	$2s^2\ 2p\ 3d\ ^3D_1 \rightarrow 2s^2\ 2p^2\ ^3P_1$	7.00	14 ± 10	Y
27b	···	12.42	Fe XXI	$2s^2\ 2p\ 3d\ ^3D_2 \rightarrow 2s^2\ 2p^2\ ^3P_1$	7.00	···	
28	12.45	12.44	Ni XIX	$2p^5\ 3d\ ^1P_1 \rightarrow 2p^6\ ^1S_0$	6.90	30 ± 10	Y
29	12.54	12.52	Fe XXI	$2s^2\ 2p\ 3d\ ^3F_3 \rightarrow 2s^2\ 2p^2\ ^3P_2$	7.00	27 ± 10	
30	12.60	12.59	Fe XXI	$2s^2\ 2p\ 3d\ ^3F_2 \rightarrow 2s^2\ 2p^2\ ^3P_2$	7.00	27 ± 10	
31a	12.84	12.82	Fe XX	$2s^2\ 2p^2\ (^3P)\ 3d\ ^4P_{5/2} \rightarrow 2s^2\ 2p^3\ ^4S_{3/2}$	7.00	83 ± 13	Y
31b	···	12.83	Fe XX	$2s^2\ 2p^2\ (^3P)\ 3d\ ^4P_{1/2} \rightarrow 2s^2\ 2p^3\ ^4S_{3/2}$	7.00	···	
31c	···	12.83	Fe XX	$2s^2\ 2p^2\ (^3P)\ 3d\ ^4P_{3/2} \rightarrow 2s^2\ 2p^3\ ^4S_{3/2}$	7.00	···	
32	13.41	13.42	Fe XIX	$2p^3\ (^2D)\ 3d\ ^1F_3 \rightarrow 2s^2\ 2p^4\ ^3P_2$	6.90	26 ± 12	
33a	13.45	13.45	Ne IX	$1s\ 2p\ ^1P_1 \rightarrow 1s^2\ ^1S_0$	6.60	281 ± 22	Y
33b	···	13.46	Fe XIX	$2p^3\ (^2D)\ 3d\ ^3D_1 \rightarrow 2s^2\ 2p^4\ ^3P_0$	6.90	···	
33c	···	13.46	Fe XIX	$2p^3\ (^2D)\ 3d\ ^3S_1 \rightarrow 2s^2\ 2p^4\ ^3P_2$	6.90	···	
34	13.49	13.50	Fe XIX	$2p^3\ (^2P)\ 3d\ ^1D_2 \rightarrow 2s^2\ 2p^4\ ^3P_2$	6.90	48 ± 17	
35a	13.52	13.51	Fe XXI	$2s\ 2p^2\ (^4P)\ 3s\ ^3P_0 \rightarrow 2s\ 2p^3\ ^3D_1$	7.00	15 ± 15	
35b	···	13.52	Fe XIX	$2p^3\ (^2D)\ 3d\ ^3D_3 \rightarrow 2s^2\ 2p^4\ ^3P_2$	6.90	···	
36a	13.55	13.53	Fe XIX	$2p^3\ (^2D)\ 3d\ ^3D_2 \rightarrow 2s^2\ 2p^4\ ^3P_2$	6.90	120 ± 16	
36b	···	13.55	Ne IX	$1s\ 2p\ ^3P_2 \rightarrow 1s^2\ ^1S_0$	6.55	···	
36c	···	13.55	Fe XIX	$2p^3\ (^2P)\ 3d\ ^3D_2 \rightarrow 2s^2\ 2p^4\ ^3P_1$	6.90	···	
36d	···	13.55	Ne IX	$1s\ 2p\ ^3P_1 \rightarrow 1s^2\ ^1S_0$	6.55	···	
37a	13.67	13.65	Fe XIX	$2p^3\ (^2D)\ 3d\ ^3F_3 \rightarrow 2s^2\ 2p^4\ ^3P_2$	6.90	30 ± 13	
37b	···	13.66	Fe XIX	$2p^3\ (^2D)\ 3d\ ^1P_1 \rightarrow 2s^2\ 2p^4\ ^3P_2$	6.90	···	
38	13.71	13.70	Ne IX	$1s\ 2s\ ^3S_1 \rightarrow 1s^2\ ^1S_0$	6.60	182 ± 18	
39a	13.74	13.74	Fe XIX	$2p^3\ (^2D)\ 3d\ ^3P_2 \rightarrow 2s^2\ 2p^4\ ^3P_1$	6.90	~ 5	
39b	···	13.74	Fe XIX	$2p^3\ (^2D)\ 3d\ ^1F_3 \rightarrow 2s^2\ 2p^4\ ^1D_2$	6.90	···	
39c	···	13.74	Fe XX	$2s^2\ 2p^2\ (^3P)\ 3s\ ^4P_{5/2} \rightarrow 2s^2\ 2p^3\ ^4S_{3/2}$	7.00	···	
40a	13.78	13.78	Fe XIX	$2p^3\ (^2D)\ 3d\ ^3S_1 \rightarrow 2s^2\ 2p^4\ ^1D_2$	6.90	54 ± 12	
40b	···	13.78	Ni XIX	$2p^5\ 3s\ ^1P_1 \rightarrow 2p^6\ ^1S_0$	6.80	···	
40c	···	13.80	Fe XIX	$2p^3\ (^4S)\ 3d\ ^3D_3 \rightarrow 2s^2\ 2p^4\ ^3P_2$	6.90	···	
41	13.84	13.82	Fe XVII	$2s\ 2p^6\ 3p\ ^1P_1 \rightarrow 2p^6\ ^1S_0$	6.80	41 ± 11	
42a	14.06	14.04	Ni XIX	$2p^5\ 3s\ ^3P_1 \rightarrow 2p^6\ ^1S_0$	6.80	50 ± 11	Y
42b	···	14.08	Ni XIX	$2p^5\ 3s\ ^3P_2 \rightarrow 2p^6\ ^1S_0$	6.80	···	
43a	14.19	14.20	Fe XVIII	$2p^4\ (^1D)\ 3d\ ^2D_{5/2} \rightarrow 2s^2\ 2p^5\ ^2P_{3/2}$	6.90	53 ± 13	
43b	···	14.21	Fe XVIII	$2p^4\ (^1D)\ 3d\ ^2P_{3/2} \rightarrow 2s^2\ 2p^5\ ^2P_{3/2}$	6.90	···	
44	14.23	14.26	Fe XVIII	$2p^4\ (^1D)\ 3d\ ^2S_{1/2} \rightarrow 2s^2\ 2p^5\ ^2P_{3/2}$	6.90	64 ± 14	
45a	14.27	14.27	Fe XVIII	$2p^4\ (^1D)\ 3d\ ^2F_{5/2} \rightarrow 2s^2\ 2p^5\ ^2P_{3/2}$	6.90	29 ± 12	
45b	···	14.27	Fe XX	$2s\ 2p^3\ (^5S)\ 3s\ ^4S_{3/2} \rightarrow 2s\ 2p^4\ ^4P_{5/2}$	7.00	···	
46	14.32	14.34	Fe XVIII	$2p^4\ (^1D)\ 3d\ ^2P_{1/2} \rightarrow 2s^2\ 2p^5\ ^2P_{1/2}$	6.90	27 ± 11	

Table 3. Continued

$Label^a$	$\lambda^b_{\rm obs}$	$\lambda^b_{\rm pred}$	Ion	Transition (*upper* → *lower*)	$\log T^c_{\rm max}$	$(F \pm \sigma)^d$	EM^e
47a	14.37	14.36	Fe XVIII	$2p^4\ (^1D)\ 3d\ ^2D_{3/2}\ \rightarrow\ 2s^2\ 2p^5\ ^2P_{1/2}$	6.90	64 ± 13	Y
47b	⋯	14.37	Fe XVIII	$2p^4\ (^3P)\ 3d\ ^2D_{5/2}\ \rightarrow\ 2s^2\ 2p^5\ ^2P_{3/2}$	6.90	⋯	
48a	14.43	14.41	Fe XX	$2s\ 2p^3\ (^5S)\ 3s\ ^4S_{3/2}\ \rightarrow\ 2s\ 2p^4\ ^4P_{3/2}$	7.00	46 ± 11	
48b	⋯	14.42	Fe XVIII	$2p^4\ (^1D)\ 3d\ ^2P_{3/2}\ \rightarrow\ 2s^2\ 2p^5\ ^2P_{1/2}$	6.90	⋯	
49a	14.51	14.48	Fe XVIII	$2p^4\ (^3P)\ 3d\ ^4F_{5/2}\ \rightarrow\ 2s^2\ 2p^5\ ^2P_{3/2}$	6.90	30 ± 11	
49b	⋯	14.51	Fe XX	$2s^2\ 2p^2\ (^1D)\ 3p\ ^2P_{3/2}\ \rightarrow\ 2s\ 2p^4\ ^4P_{1/2}$	7.00	⋯	
50a	14.55	14.53	Fe XVIII	$2p^4\ (^3P)\ 3d\ ^2F_{5/2}\ \rightarrow\ 2s^2\ 2p^5\ ^2P_{3/2}$	6.90	57 ± 12	Y
50b	⋯	14.55	Fe XVIII	$2p^4\ (^3P)\ 3d\ ^4P_{3/2}\ \rightarrow\ 2s^2\ 2p^5\ ^2P_{3/2}$	6.90	⋯	
50c	⋯	14.58	Fe XVIII	$2p^4\ (^3P)\ 3d\ ^4P_{1/2}\ \rightarrow\ 2s^2\ 2p^5\ ^2P_{3/2}$	6.90	⋯	
51	15.02	15.02	Fe XVII	$2p^5\ 3d\ ^1P_1\ \rightarrow\ 2p^6\ ^1S_0$	6.75	330 ± 22	Y
52	15.09	15.08	Fe XIX	$2s\ 2p^4\ (^4P)\ 3s\ ^3P_2\ \rightarrow\ 2s\ 2p^5\ ^3P_2$	6.90	47 ± 13	
53a	15.16	15.18	O VIII	$4p\ ^2P_{3/2}\ \rightarrow\ 1s\ ^2S_{1/2}$	6.50	29 ± 12	
53b	⋯	15.18	O VIII	$4p\ ^2P_{1/2}\ \rightarrow\ 1s\ ^2S_{1/2}$	6.50	⋯	
54	15.19	15.20	Fe XIX	$2p^3\ (^4S)\ 3s\ ^5S_2\ \rightarrow\ 2s^2\ 2p^4\ ^3P_2$	6.90	72 ± 14	
55	15.27	15.26	Fe XVII	$2p^5\ 3d\ ^3D_1\ \rightarrow\ 2p^6\ ^1S_0$	6.75	133 ± 15	Y
56	15.44	15.45	Fe XVII	$2p^5\ 3d\ ^3P_1\ \rightarrow\ 2p^6\ ^1S_0$	6.70	29 ± 10	
57	15.49	15.50	Fe XVIII	$2s\ 2p^5\ (^1P)\ 3s\ ^2P_{3/2}\ \rightarrow\ 2s\ 2p^6\ ^2S_{1/2}$	6.90	19 ± 9	
58	15.62	15.63	Fe XVIII	$2p^4\ (^1D)\ 3s\ ^2D_{5/2}\ \rightarrow\ 2s^2\ 2p^5\ ^2P_{3/2}$	6.90	31 ± 10	
59	15.66	15.63	Fe XX	$2s^2\ 2p^2\ (^1D)\ 3p\ ^2P_{3/2}\ \rightarrow\ 2s\ 2p^4\ ^2P_{1/2}$	7.00	16 ± 9	
60	15.78	15.77	Fe XVIII	$2p^4\ (^3P)\ 3s\ ^2P_{1/2}\ \rightarrow\ 2s^2\ 2p^5\ ^2P_{3/2}$	6.90	19 ± 9	
61	15.83	15.83	Fe XVIII	$2p^4\ (^3P)\ 3s\ ^4P_{3/2}\ \rightarrow\ 2s^2\ 2p^5\ ^2P_{3/2}$	6.90	23 ± 10	
62a	15.88	15.84	Fe XX	$2s^2\ 2p^2\ (^3P)\ 3p\ ^2P_{3/2}\ \rightarrow\ 2s\ 2p^4\ ^2P_{3/2}$	7.00	42 ± 11	
62b	⋯	15.85	Fe XVIII	$2p^4\ (^3P)\ 3s\ ^4P_{1/2}\ \rightarrow\ 2s^2\ 2p^5\ ^2P_{3/2}$	6.90	⋯	
62c	⋯	15.87	Fe XVIII	$2p^4\ (^1D)\ 3s\ ^2D_{3/2}\ \rightarrow\ 2s^2\ 2p^5\ ^2P_{1/2}$	6.80	⋯	
63a	16.01	16.00	Fe XVIII	$2p^4\ (^3P)\ 3s\ ^2P_{3/2}\ \rightarrow\ 2s^2\ 2p^5\ ^2P_{3/2}$	6.90	219 ± 19	Y
63b	⋯	16.01	O VIII	$3p\ ^2P_{3/2}\ \rightarrow\ 1s\ ^2S_{1/2}$	6.50	⋯	
63c	⋯	16.01	O VIII	$3p\ ^2P_{1/2}\ \rightarrow\ 1s\ ^2S_{1/2}$	6.50	⋯	
64	16.07	16.07	Fe XVIII	$2p^4\ (^3P)\ 3s\ ^4P_{5/2}\ \rightarrow\ 2s^2\ 2p^5\ ^2P_{3/2}$	6.90	94 ± 14	
65a	16.20	16.17	Fe XVIII	$2s\ 2p^5\ (^3P)\ 3s\ ^2P_{3/2}\ \rightarrow\ 2s\ 2p^6\ ^2S_{1/2}$	6.90	29 ± 9	
65b	⋯	16.24	Fe XVII	$2p^5\ 3p\ ^3P_2\ \rightarrow\ 2p^6\ ^1S_0$	6.70	⋯	
66a	16.32	16.31	Fe XVIII	$2s\ 2p^5\ (^3P)\ 3s\ ^4P_{3/2}\ \rightarrow\ 2s\ 2p^6\ ^2S_{1/2}$	6.90	22 ± 9	
66b	⋯	16.34	Fe XVII	$2p^5\ 3p\ ^3D_2\ \rightarrow\ 2p^6\ ^1S_0$	6.70	⋯	
67	16.77	16.78	Fe XVII	$2p^5\ 3s\ ^3P_1\ \rightarrow\ 2p^6\ ^1S_0$	6.70	188 ± 17	Y
68	17.05	17.05	Fe XVII	$2p^5\ 3s\ ^1P_1\ \rightarrow\ 2p^6\ ^1S_0$	6.70	225 ± 20	Y
69	17.09	17.10	Fe XVII	$2p^5\ 3s\ ^3P_2\ \rightarrow\ 2p^6\ ^1S_0$	6.70	181 ± 19	Y
70	17.62	17.66	Fe XVIII	$2p^4\ (^1D)\ 3p\ ^2P_{3/2}\ \rightarrow\ 2s\ 2p^6\ ^2S_{1/2}$	6.90	38 ± 10	
71	17.79	17.77	O VII	$1s\ 4p\ ^1P_1\ \rightarrow\ 1s^2\ ^1S_0$	6.35	36 ± 10	
72	18.63	18.63	O VII	$1s\ 3p\ ^1P_1\ \rightarrow\ 1s^2\ ^1S_0$	6.35	51 ± 11	Y

Table 3. Continued

$Label^a$	$\lambda^b_{\rm obs}$	$\lambda^b_{\rm pred}$	Ion	Transition (*upper* → *lower*)	$\log T^c_{\rm max}$	$(F \pm \sigma)^d$	EM^e
73a	18.96	18.97	O VIII	$2p\ ^2P_{3/2} \rightarrow 1s\ ^2S_{1/2}$	6.50	1214 ± 38	Y
73b	···	18.97	O VIII	$2p\ ^2P_{1/2} \rightarrow 1s\ ^2S_{1/2}$	6.50	···	
74a	20.90	20.91	N VII	$3p\ ^2P_{3/2} \rightarrow 1s\ ^2S_{1/2}$	6.35	21 ± 8	Y
74b	···	20.91	N VII	$3p\ ^2P_{1/2} \rightarrow 1s\ ^2S_{1/2}$	6.35	···	
75	21.61	21.60	O VII	$1s\,2p\ ^1P_1 \rightarrow 1s^2\ ^1S_0$	6.30	283 ± 20	Y
76a	21.81	21.80	O VII	$1s\,2p\ ^3P_2 \rightarrow 1s^2\ ^1S_0$	6.30	59 ± 11	
76b	···	21.81	O VII	$1s\,2p\ ^3P_1 \rightarrow 1s^2\ ^1S_0$	6.30	···	
77	22.10	22.10	O VII	$1s\,2s\ ^3S_1 \rightarrow 1s^2\ ^1S_0$	6.30	185 ± 17	
78a	24.26	24.20	S XIV	$1s^2\,4d\ ^2D_{3/2} \rightarrow 1s^2\,2p\ ^2P_{1/2}$	6.50	30 ± 9	
78b	···	24.28	S XIV	$1s^2\,4d\ ^2D_{5/2} \rightarrow 1s^2\,2p\ ^2P_{3/2}$	6.50	···	
79a	24.78	24.78	N VII	$2p\ ^2P_{3/2} \rightarrow 1s\ ^2S_{1/2}$	6.30	126 ± 15	Y
79b	···	24.78	N VII	$2p\ ^2P_{1/2} \rightarrow 1s\ ^2S_{1/2}$	6.30	···	
80a	28.46	28.47	C VI	$3p\ ^2P_{3/2} \rightarrow 1s\ ^2S_{1/2}$	6.20	31 ± 9	Y
80b	···	28.47	C VI	$3p\ ^2P_{1/2} \rightarrow 1s\ ^2S_{1/2}$	6.20	···	
81	28.79	28.79	N VI	$1s\,2p\ ^1P_1 \rightarrow 1s^2\ ^1S_0$	6.20	38 ± 10	Y
82	28.92		No Id	...		17 ± 8	
83	29.10	29.08	N VI	$1s\,2p\ ^3P_1 \rightarrow 1s^2\ ^1S_0$	6.15	34 ± 9	
84	29.30	29.32	S XV	$1s\,3d\ ^1D_2 \rightarrow 1s\,2p\ ^1P_1$	7.20	26 ± 9	
85	29.53	29.53	N VI	$1s\,2s\ ^3S_1 \rightarrow 1s^2\ ^1S_0$	6.15	25 ± 9	Y
86	33.56	33.55	S XIV	$1s^2\,3s\ ^2S_{1/2} \rightarrow 1s^2\,2p\ ^2P_{3/2}$	6.50	39 ± 10	Y
87a	33.74	33.73	C VI	$2p\ ^2P_{3/2} \rightarrow 1s\ ^2S_{1/2}$	6.20	226 ± 18	Y
87b	···	33.74	C VI	$2p\ ^2P_{1/2} \rightarrow 1s\ ^2S_{1/2}$	6.20	···	
88	36.40		Fe XVII + Ne X Lyα 3rd order			44 ± 10	
89a	36.57	36.56	S XII	$2s^2\,3d\ ^2D_{5/2} \rightarrow 2s^2\,2p\ ^2P_{3/2}$	6.40	24 ± 9	Y
89b	···	36.57	S XII	$2s^2\,3d\ ^2D_{3/2} \rightarrow 2s^2\,2p\ ^2P_{3/2}$	6.40	···	
90	37.94	37.92	Mg XI ?	$1s\,4p\ ^3P_2 \rightarrow 1s\,2s\ ^3S_1$	6.80	56 ± 11	
91	40.31	40.27	C V	$1s\,2p\ ^1P_1 \rightarrow 1s^2\ ^1S_0$	6.00	38 ± 10	Y
92	43.76	43.76	Si XI	$2s\,3p\ ^1P_1 \rightarrow 2s^2\ ^1S_0$	6.20	55 ± 11	Y
93	44.01	44.02	Si XII	$1s^2\,3d\ ^2D_{3/2} \rightarrow 1s^2\,2p\ ^2P_{1/2}$	6.30	52 ± 11	Y
94	44.16	44.17	Si XII	$1s^2\,3d\ ^2D_{5/2} \rightarrow 1s^2\,2p\ ^2P_{3/2}$	6.30	115 ± 14	Y
95	45.50	45.52	Si XII	$1s^2\,3s\ ^2S_{1/2} \rightarrow 1s^2\,2p\ ^2P_{1/2}$	6.30	49 ± 11	
96	45.68	45.69	Si XII	$1s^2\,3s\ ^2S_{1/2} \rightarrow 1s^2\,2p\ ^2P_{3/2}$	6.30	57 ± 11	Y
97	46.30	46.30	Si XI	$2s\,3d\ ^3D_2 \rightarrow 2s\,2p\ ^3P_1$	6.20	31 ± 10	
98	46.42	46.40	Si XI	$2s\,3d\ ^3D_3 \rightarrow 2s\,2p\ ^3P_2$	6.20	41 ± 10	Y
99	49.17	49.18	Si XI	$2s\,3s\ ^3S_1 \rightarrow 2s\,2p\ ^3P_2$	6.20	28 ± 10	
100	49.20	49.22	Si XI	$2s\,3d\ ^1D_2 \rightarrow 2s\,2p\ ^1P_1$	6.20	35 ± 11	
101	50.33		Fe XVII λ 16.78 3rd order			52 ± 11	
102	56.90		O VIII Lyα 3rd order			65 ± 11	
103	57.71		No Id	...		23 ± 9	
104	66.30	66.25	Fe XVI	$4f\ ^2F_{5/2} \rightarrow 3d\ ^2D_{3/2}$	6.50	23 ± 9	

Table 3. Continued

$Label^a$	$\lambda^b_{\rm obs}$	$\lambda^b_{\rm pred}$	Ion	Transition (*upper* → *lower*)	$\log T^c_{\rm max}$	$(F \pm \sigma)^d$	EM^e
105	66.37	66.36	Fe XVI	$4f\ ^2F_{7/2} \rightarrow 3d\ ^2D_{5/2}$	6.50	36 ± 10	Y
106	88.09	88.08	Ne VIII	$1s^2\ 3p\ ^2P_{3/2} \rightarrow 1s^2\ 2s\ ^2S_{1/2}$	5.80	37 ± 10	Y
107	88.14	88.12	Ne VIII	$1s^2\ 3p\ ^2P_{1/2} \rightarrow 1s^2\ 2s\ ^2S_{1/2}$	5.80	40 ± 10	Y
108	93.96	93.92	Fe XVIII	$2s\ 2p^6\ ^2S_{1/2} \rightarrow 2s^2\ 2p^5\ ^2P_{3/2}$	6.80	60 ± 11	
109a	98.29	98.26	Ne VIII	$1s^2\ 3d\ ^2D_{5/2} \rightarrow 1s^2\ 2p\ ^2P_{3/2}$	5.80	34 ± 9	
109b	⋯	98.27	Ne VIII	$1s^2\ 3d\ ^2D_{3/2} \rightarrow 1s^2\ 2p\ ^2P_{3/2}$	5.80	⋯	
110	108.41	108.36	Fe XIX	$2s\ 2p^5\ ^3P_2 \rightarrow 2s^2\ 2p^4\ ^3P_2$	6.90	48 ± 10	
111	109.99	109.95	Fe XIX	$2s\ 2p^5\ ^3P_1 \rightarrow 2s^2\ 2p^4\ ^3P_0$	6.90	10 ± 7	
112a	110.65	110.63	Fe XX	$2s\ 2p^4\ ^2D_{3/2} \rightarrow 2s^2\ 2p^3\ ^2D_{3/2}$	7.00	9 ± 7	
112b	⋯	110.63	Ne VII	$2p\ 3d\ ^3D_3 \rightarrow 2p^2\ ^3P_2$	5.80	⋯	
113	114.47	114.41	Fe XXII	$2s\ 2p^2\ ^2P_{3/2} \rightarrow 2s^2\ 2p\ ^2P_{3/2}$	7.10	10 ± 7	
114	117.16	117.18	Fe XXII	$2s\ 2p^2\ ^2P_{1/2} \rightarrow 2s^2\ 2p\ ^2P_{1/2}$	7.10	33 ± 9	
115	121.21	121.20	Fe XXI	$2s\ 2p^3\ ^3P_2 \rightarrow 2s^2\ 2p^2\ ^3P_2$	7.00	12 ± 7	
116	121.85	121.84	Fe XX	$2s\ 2p^4\ ^4P_{3/2} \rightarrow 2s^2\ 2p^3\ ^4S_{3/2}$	7.00	19 ± 8	
117	128.81	128.75	Fe XXI	$2s\ 2p^3\ ^3D_1 \rightarrow 2s^2\ 2p^2\ ^3P_0$	7.00	35 ± 9	Y
118	132.92	132.84	Fe XX	$2s\ 2p^4\ ^4P_{5/2} \rightarrow 2s^2\ 2p^3\ ^4S_{3/2}$	7.00	24 ± 9	
119	132.96	132.91	Fe XXIII	$2s\ 2p\ ^1P_1 \rightarrow 2s^2\ ^1S_0$	7.10	39 ± 10	Y
120	135.88	135.76	Fe XXII	$2s\ 2p^2\ ^2D_{3/2} \rightarrow 2s^2\ 2p\ ^2P_{1/2}$	7.10	17 ± 8	

[a] Invididual components of unresolved line blends are indicated by letters.

[b] Observed and predicted (CHIANTI database) wavelengths.

[c] Maximum emissivity temperature in K.

[d] Total line counts and errors.

[e] Lines selected to derive the emission measure distribution.

contaminating iron line because all of the other prominent Fe XVII lines in the spectrum are well predicted (within a factor 1.5). Other possible explanations include optical thickness effects due to resonant line scattering (Testa et al. 2004) or uncertainties in the theoretical line ratios due to processes of population of the excited atomic levels not taken into account by the adopted line emissivity code (Smith et al. 2002).

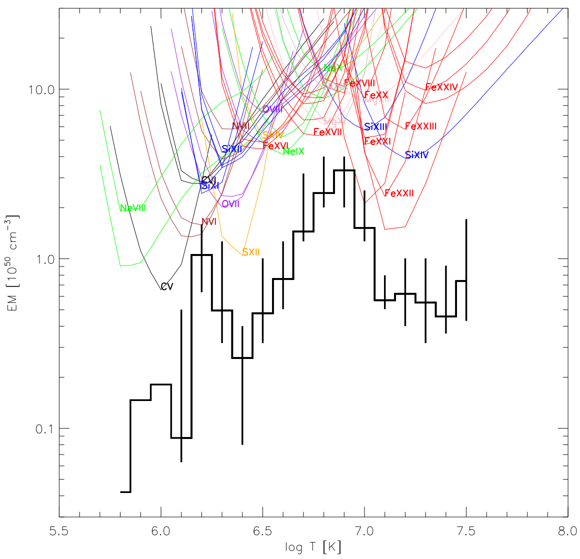

Fig. 3.— Emission measure distribution (solid histogram) vs. temperature and inverse line emissivity curves, scaled by the individual element abundances relative to iron. Representative ion labels are placed at the relevant peak emissivity temperature. In the electronic edition, the colors of the emissivity curves indicate different elements (C black, N brown, O purple, Ne green, Mg pink, Si blue, S orange, Fe red, Ni gray).

The final EMD is shown in Fig. 3, together with the inverse emissivity curves computed with the set of abundances (relative to Fe) reported in Table 4. Note that the available data allow us to constrain the emission measure distribution in the temperature range $\log T \sim 6.0$–7.5 K. Note also that if the Ne X Lyα doublet is used for the emission measure analysis, the resulting EMD in the temperature range $\log T$ 6.4–6.9 K turns out to be flatter than the one in Fig. 3, but compatible within formal uncertainties, and the Ne/Fe abundance ratio lower by a factor 1.6 ($Ne/Fe \sim 3$ using the Ne X Lyα, rather than $Ne/Fe \lesssim 5$).

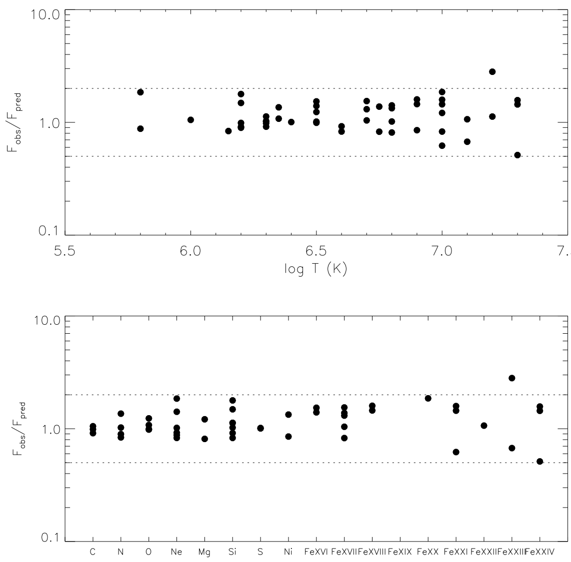

Fig. 4.— Ratios of observed to predicted line fluxes vs. temperature (upper panel) and vs. ionization stage (lower panel). The symbols refer to lines with relatively high S/N ratio selected for the emission measure analysis; the agreement between measurements and model predictions is generally within a factor 2 (dotted horizontal lines).

The appropriateness of our solution can be best appreciated from inspection of Fig. 4 where the ratio of observed to predicted line counts vs. temperature and vs. ionization species is shown: the agreement is within a factor 2 for all of the selected lines, with the exception of the Fe XXII line at λ 11.75 Å. A more general qualitative comparison of the observed and predicted model spectrum (folded with the analytical line spread function used for line fitting) shows a good overall agreement, but also some deficiency of the CHIANTI spectrum in several spectral regions populated by many, relatively weak emission lines from L-shell transitions of Fe XVII– XIX ions: in particular, we note the 10–12 Å range – where the most prominent Fe XXIV lines are located, but where several contaminating lines from lower ionization species are missing from the CHIANTI database – and the region of the Ne IX triplet (13.4–13.8 Å), where similar incompleteness effects are visible. By employing the Astrophysical Plasma Emission Database (APED) V1.3 line list and emissivities, we have verified that our EMD and chemical abundances yield a predicted spectrum that matches the available data better in both wavelength regions mentioned above. The robustness of our solution derives from the careful selection of strong and reliable lines for the emission measure analysis.

In order to determine the Fe/H ratio in the corona of AD Leo, we have performed a detailed comparison (Fig. 5) between the observed continuum emission level and that predicted with different assumptions of the plasma metallicity, Z. In fact, the relative line to continuum ratio increases with increasing Z, while the volume emission measure needs to be scaled down by the same factor in order to keep the total predicted source flux constant. A close inspection of the spectral regions 6–9 Å, 18–21 Å, and 44–54 Å, where the continuum is more visible, suggests a metallicity larger than $0.8 Z_{\odot}$ for the corona of AD Leo; as explained in Sect. A.3, this relatively high value implies that the Fe/H ratio cannot be determined to within less than a factor 2 (Table 4).

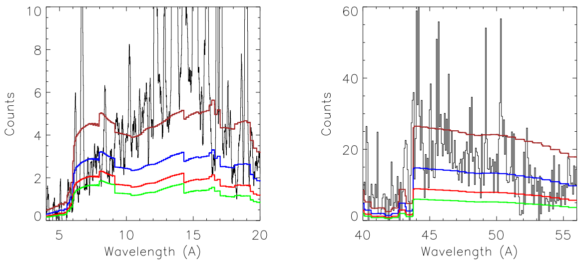

Fig. 5.— Comparison between the observed spectrum (with a bin size of 0.075 Å) and the continuum emission level predicted for different values of the Fe/H abundance, with the four stacked curves corresponding from top to bottom to: 0.2, 0.4, 0.8, and 1.6 times the solar metallicity (brown, blue, red, and green, respectively, in the electronic edition).

The *Chandra* LETG spectrum of AD Leo allowed us to estimate the plasma density at different temperatures from sensitive line ratios derived from the O VII, Ne IX, and Si XIII He-like triplets, and also from Fe XX, Fe XXI, and Fe XXII lines. The details of the analysis are described in Sect. A.4, and the main results are reported in Table 5.

Table 4
Coronal abundances in AD Leo

	FIP eV	N[a]	A_Z/A_H[b]	$A_Z/A_{Z\odot}$[c]
C	11.26	3	$(9.6^{+3.3}_{-1.4}) \times 10^{-4}$	$2.7^{+0.9}_{-0.4}$
N	14.53	4	$(3.0^{+1.0}_{-0.5}) \times 10^{-4}$	$3.3^{+1.1}_{-0.5}$
O	13.62	4	$(1.6^{+0.5}_{-0.3}) \times 10^{-3}$	$2.1^{+0.7}_{-0.4}$
Ne	21.56	6	$(5.6^{+0.9}_{-1.5}) \times 10^{-4}$	$4.7^{+0.7}_{-1.3}$
Mg	7.65	2	$(3.0^{+2.1}_{-0.5}) \times 10^{-5}$	$0.8^{+0.6}_{-0.1}$
Si	8.15	7	$(9.0^{+1.3}_{-2.5}) \times 10^{-5}$	$2.5^{+0.4}_{-0.7}$
S	10.36	2	$(1.1^{+1.0}_{-1.4}) \times 10^{-4}$	$6.6^{+6.0}_{-1.6}$
Ni	7.64	2	$(3.4^{+0.7}_{-1.4}) \times 10^{-6}$	$1.9^{+0.4}_{-0.8}$
Fe[d]	7.90	18	$2.6 - 5.2 \times 10^{-5}$	$0.8 - 1.6$

[a]Number of spectral lines of the relevant element included in the emission measure reconstruction.

[b]Element abundances relative to hydrogen.

[c]Element abundances relative to the solar ones (Grevesse et al. 1992).

[d]Abundance range determined by matching the continuum (Sect. A.3).

Table 5

Density and temperature spectroscopic diagnostics[a]

Ion	R_D[b]	N_e cm^{-3}	R_T[c]	$\log T$ K	$\log T_{max}$[d] K	P[e] dyn cm^{-2}
O VII	3.15 ± 0.68	$(7.1^{+8.2}_{-6.0}) \times 10^9$	0.86 ± 0.12	6.29 ± 0.12	6.3	$3.8^{+7.0}_{-3.4}$
Ne IX	1.88 ± 0.37	$(3.9^{+3.7}_{-1.6}) \times 10^{11}$	1.02 ± 0.15	< 6.44	6.6	$< 3 \times 10^2$
Si XIII	0.92 ± 0.38	$(9.8^{+9.2}_{-6.1}) \times 10^{13}$	1.03 ± 0.35	< 6.90	7.0	$< 4 \times 10^5$
Fe XXI	0.35 ± 0.22	$(1.8^{+2.3}_{-1.5}) \times 10^{12}$	$\cdots$	7.02[f]	7.0	$5^{+7}_{-4} \times 10^3$

[a]Statistical uncertainties are all at the 1σ confidence level

[b]Density sensitive f/i line ratios

[c]Temperature sensitive (f+i)/r line ratios

[d]Peak emissivity temperature

[e]Plasma pressure, $P = 2N_e k_B T$

[f]Average temperature, weighted by the line emissivity and the emission measure distribution vs. temperature

5. Discussion

5.1. Plasma thermal structure and abundances

Our reconstructed EMD indicates that the corona of AD Leo is dominated by plasma in the temperature range 3×10^6 – 10^7 K, in qualitative agreement with previous results based on EUVE and SAX data (Cully et al. 1997; Sciortino et al. 1999), but a sizeable fraction ($\sim 20\%$) of the plasma volume emission measure is at higher temperatures (up to ~ 30 MK; see also van den Besselaar et al. 2003). Figure 6 shows a comparison with the three EMDs derived by Sanz Forcada & Micela (2002) during quiescent and low-amplitude flaring phases of AD Leo, and in its average state (based on the sum of all the nine EUVE spectra discussed by these authors). Our *Chandra* EMD turns out to be remarkably similar to the latter, but higher by a factor $\lesssim 2$ in the temperature range 3–6 MK. The overall agreement between these EMDs, based on data of different instruments and derived with different procedures, strengthens our confidence in the results of the line-based emission measure analysis. This also suggests that the corona of AD Leo has maintained nearly the same configuration on time scales of about 10 years.

The EMD of AD Leo appears similar to that of other active late-type stars but is significantly less steep. The volume emission measure increases as T^β in the range $\log T = 6.4$–6.9, with $\beta = 2.2 \pm 1.1$, as compared with slopes $\beta = 4$–6 observed in RS CVn-type binaries (Griffiths & Jordan 1998; Sanz Forcada, Brickhouse, & Dupree 2003; Argiroffi, Maggio, & Peres 2003), and also in single late-type dwarfs and yellow giants (Ayres et al. 1998; Drake et al. 2000; Scelsi et al. 2003). This result implies that the bulk of the X-ray emission of AD Leo can be explained by plasma confined in static, constant cross-section and uniformly-heated coronal loop structures (see also below). Before attempting an interpretation with such a model, however, we must address the issue of the coronal abundances.

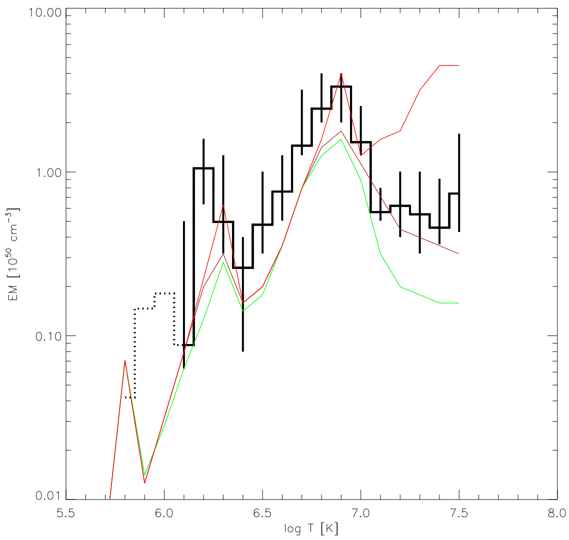

Fig. 6.— Comparison between the *Chandra* emission measure distribution (thick-line histogram) and the three distributions derived by Sanz Forcada & Micela (2002) during quiescent, average, and flaring phases (from bottom to top, and colored green, brown, and red in the electronic edition), based on EUVE observations taken between 1993 and 2000.

Abundances in the corona of AD Leo (Table 4) are all larger than the solar photospheric values of Grevesse et al. (1992) by factors of 2–4, with the exception of Mg and Fe, whose abundances are solar within errors, and of S, which appears overabundant compared to the solar mixture. These chemical abundances when sorted by the First Ionization Potential (FIP) of each element reveal the characteristic pattern shown in Fig. 7. In the solar corona, and in particular in long-lived coronal structures, the composition of the plasma appears enriched by low-FIP elements (FIP $< 10\,\mathrm{eV}$) by about a factor 4 (on average) with respect to photospheric values (Feldman & Laming 2000), while in other stars a more complex behavior has been observed (Drake 2003; Sanz Forcada, Favata, & Micela 2004), with a tendency for the low-FIP elements (including iron) to become depleted with respect to the high-FIP elements (Neon in particular) in extremely active RS CVn-type and Algol-type binaries. At face value, in the corona of AD Leo there is some evidence for a FIP-related bias in the abundances, similar to that of other stars with high activity levels, although abundances relative to stellar *photospheric* values should be employed to confirm such a trend.

Unfortunately, stellar photospheric spectra of dM stars are notoriously difficult to analyze, and firm measurements of photospheric abundances in AD Leo are limited to studies by Naftilan, Sandmann, & Pettersen (1992) and Jones et al. (1996), who estimate $[Fe/H] = -0.47$ and $[Fe/H] = -0.75 \pm 0.25$, respectively. These values can probably be revised upward by 0.17 dex compared to our abundances: in the case of Jones et al. (1996) it is not clear which solar Fe abundance was assumed, though Naftilan et al. (1992) adopted $\log A_{\mathrm{Fe}} = 7.67$ (in the conventional spectroscopic logarithmic units), compared to

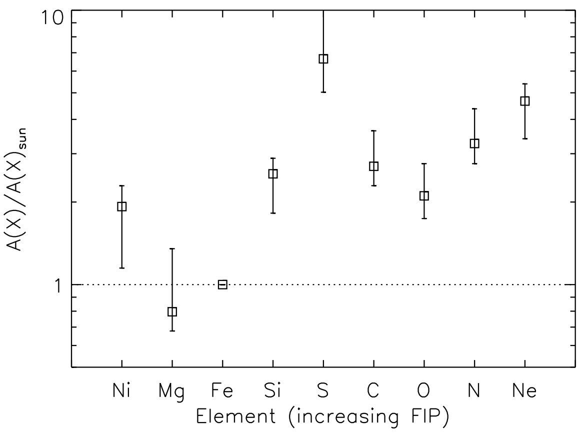

Fig. 7.— Pattern of coronal abundances (relative to solar values) vs. chemical element sorted by First Ionization Potential, assuming solar Fe abundance (for different Fe values, all points shift by the same factor).

$\log A_{\mathrm{Fe}} = 7.51$ recommended by Grevesse et al. (1992). Both Naftilan et al. (1992) and Jones et al. (1996) remark on the apparent metal paucity of AD Leo for its apparent age: in fact, AD Leo is a population I object by its motion, and quite young by its fast rotation and enhanced activity. Our coronal abundances suggest, then, that either the corona is generally enhanced in metals relative to photosphere, or else the existing photospheric estimates are spuriously low. The latter is our preferred explanation owing to the difficulties inherent in the compositional analysis of such an active dMe star.

The most puzzling result, however, is the relatively high metallicity (represented by a nearly solar Fe/H value) suggested by the line-to-continuum ratios (Sect. 4.2 and Fig. 5) as compared to previous low resolution X-ray studies: although the result is affected by a large uncertainty, Fe/H values 0.2–0.3 times solar (Sciortino et al. 1999; Favata et al. 2000a) seem to be incompatible with our data. Drake (2002) noted that there can be a tendency of finding spuriously low abundances with global model fitting approaches as applied to lower resolution spectra: both missing line transitions in spectral models that form a pseudo-continuum and limited signal-to-noise ratio can result in line flux being interpreted as continuum. However, the size of the discrepancy between our abundance results and those derived from low resolution spectra is still surprising. We note that this uncertainty affects the absolute scale of the other element abundances but not their ratios, and also the absolute value of the plasma emission measure but not the shape of its distribution vs. temperature.

Of the individual abundance results, the high S and Si abundances are notable. With FIP= 10.36 eV, S is generally considered an intermediate FIP element, and is generally not seen to be conspicuously over- or underabundant. If the relative abundances of elements in the photosphere of AD Leo represent those of the solar mixture, as the analysis of Naftilan et al. (1992) suggests, then AD Leo would be the first active star for which a relative S enhancement larger than that of Ne has been found.

In the case of Si, an enhancement relative to Fe and Mg is particularly interesting because these elements all have very similar FIP. Drake (2002) also found evidence for variation in the coronal Si/Mg ratio in other active stars, suggesting it might be a common coronal phenomenon. An enhancement of Si relative to Fe might possibly be understood in terms of gravitational settling, owing to the different masses of these elements (e.g. Drake 2003); however, Mg and Si also have very similar masses and any fractionation mechanism based on charge, mass or charge/mass ratio would need to be very highly tuned.

5.2. Physical interpretation

A number of key studies based on previous observations at X-ray and EUV wavelengths provide us with different working hypotheses on the corona of AD Leo, and our aim is to test these against our new results. Giampapa et al. (1996) performed fits of low-resolution ROSAT PSPC spectra of AD Leo and other M-type dwarfs, together with variability analyses of their X-ray light curves, and proposed possible modeling of the results in terms of two classes of coronal structures with different plasma temperatures and surface filling factors: very small ($L \ll R_*$) magnetic loops in low-temperature ($T \sim 2 \times 10^6$ K) quiescent active regions, and possibly small ($L \lesssim R_*$), unstable (flaring), high-temperature ($T \sim 10^7$ K) loops. A few years later, a detailed coronal loop model analysis of BeppoSAX spectra was presented by Sciortino et al. (1999), who inferred that the dominant class of X-ray emitting structures was composed of loops with maximum plasma temperature $T_{\max} \sim 10^7$ K with sizes $L < 0.1 R_*$, covering no more than 1% of the stellar surface. Those data also suggested a second class of higher temperature structures that were not as well constrained as in the former class. A detailed analysis of several X-ray flares allowed Favata et al. (2000a) to measure peak temperatures of

10-50 MK and to infer sizes of the flaring loop structures spanning the range 4–13×10^9 cm (i.e., 0.15–0.5 R_*). By applying the Rosner et al. (1978) scaling laws for isobaric loops with constant cross-section and uniform heating, Favata et al. (2000a) also derived plasma pressures in the range $\approx 10^2$–10^4 dyn cm^{-2}.

The flaring loops pinpointed by Favata et al. (2000a) are compatible with the high-temperature coronal structures suggested by Giampapa et al. (1996), but they are not as compact as indicated by the loop modeling of Sciortino et al. (1999). On the other hand, it is not yet clear whether the same class of flaring loops, in their quiescent state, may explain the "stable" part of the EMD of AD Leo, or whether they only populate its high-temperature tail. Finally, the very small and cool loops found by Giampapa et al. (1996) were not probed by the other two studies, possibly due to selection effects, namely the different bandpasses of the instruments and their relative sensitivity to cool plasma emission.

A crucial new piece of information is the plasma pressure, which we have computed from the measured densities and temperatures (Table 5) consistently derived from spectroscopic diagnostics. A plot of the pressure vs. temperature is shown in Fig. 8, which includes values computed from the results of Ness et al. (2002) (based on the same *Chandra*/LETG observation), and the range of pressures spanned by the results of Sanz Forcada & Micela (2002) – who employed density-sensitive line ratios from Fe XX– XXII ions measured in EUVE spectra. The various results mentioned above are in general agreement, within 1σ

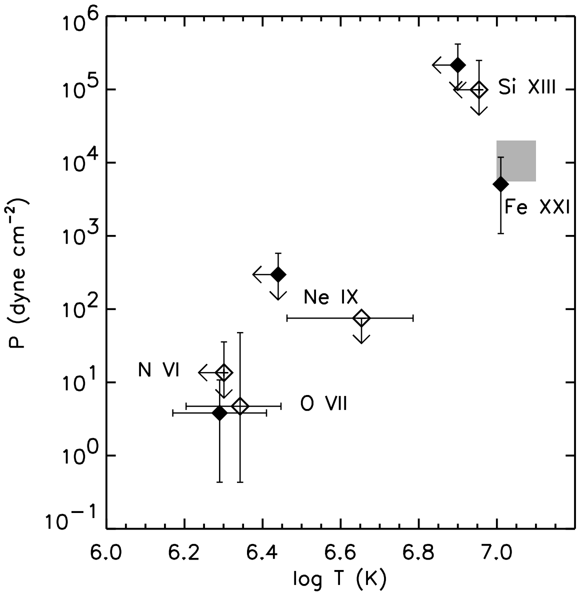

Fig. 8.— Plasma pressures (or upper limits) vs. temperature (with associated 1σ error bars) derived from density-sensitive spectroscopic diagnostics (He-like triplets and Fe XXI lines). Error bars are based on 1σ statistical uncertainties on line fluxes. Open symbols refer to measurements presented by Ness et al. (2002); shaded area shows measurements based on Fe XX–XXII line ratios derived by Sanz Forcada & Micela (2002) from EUVE spectra.

statistical uncertainties, with the exception of problematic points related to the Ne IX triplet. In particular, the densities based on ratios of Fe XXI EUV lines consistently suggest plasma pressures $\approx 10^4$ dyn cm^{-2} at $T \approx 10^7$ K; in this respect, the LETG spectrum of AD Leo resolves the concern about possible unaccounted blends of the iron lines in the lower-resolution EUVE data and confirms the previous finding based on these data. At the low temperatures ($T \approx 2 \times 10^6$ K) probed by the O VII triplet, instead, pressures of the order 1–10 dyn cm^{-2} are consistently found.

The above result raises again the issue of the pressure balance in the coronae of active stars, which we have already seen in previous works (Argiroffi et al. 2003; Sanz Forcada, Maggio, & Micela 2003). Unless the results based on spectroscopic diagnostics are affected by systematic biases due to atomic physics uncertainties, the only viable solution appears to be the existence of separate classes of coronal loops with different plasma densities, contributing to the EMD at different temperatures. As already suggested by Argiroffi et al. (2003) in the case of Capella, the high-pressure plasma could be confined in a class of loop structures having maximum temperatures near the peak of the EMD or higher, while the low-pressure plasma could be identified with structures determining the secondary EMD peak at $T \sim 2$ MK. While the latter appear similar to solar coronal active regions, the former are only observed during the short time scales of solar flares (Peres et al. 2000; Reale, Peres, & Orlando 2001).

Since the EMD of AD Leo appears very stable on time scales of several years, we conclude that the X-ray emission of this active dMe star, in its stationary state, is dominated by relatively hot and high-pressure coronal structures, with respect to solar standards. Whether these structures are in a steady or dynamic state is an issue which we address in the following section. In particular, we will consider first the hypothesis that the corona of AD Leo, at any time, is dominated by flares and then the alternative hypothesis that we are dealing with stationary (non-dynamic) coronal structures.

5.2.1. Continuous flaring hypothesis

We start by noting that the flare peak temperatures reported by Favata et al. (2000a) fall in the high-temperature tail of the present EMD, and that the pressures are also within the range we have derived from the spectral diagnostics (Tab. 5).

One way of testing the "continuous flaring" hypothesis is by looking for evidence of bulk plasma motions, as expected during the chromospheric evaporation phase. To this aim we have looked for wavelength shifts of the emission lines observed in the range 80–140Å, where the spectral resolution of the LETG is highest. Some of these lines appear redshifted by 0.02-0.05Å, corresponding to downflow velocities of the order of 10^2 km s^{-1}, but residual uncertainties in the wavelength calibration and the relatively low S/N ratio in this spectral region (see Fig. 12 in the Appendix A.1) prevent us to draw any firm conclusion.

The second test we have considered is a comparison with model predictions. Güdel et al. (2003) have recently investigated the flare rate distribution of AD Leo in EUV and X-ray radiated energy, from extensive observations with EUVE and BeppoSAX, and have derived a power-law distribution, $dN/dE \propto E^{-\alpha}$ with α in the range 2.0–2.5. This result implies that flares can play an important role in the energy budget of the corona of AD Leo. Following the limiting hypothesis that the corona is entirely heated by flares, these authors derived a time-averaged emission measure distribution with a sharp rise in temperature and a less steep decline after the EMD peak. The slopes of the ascending and descending segments depend on several parameters of the model, and in particular the low-

T part is expected to rise as $T^{2/\zeta}$, with ζ being the slope of the power-law dependence of the plasma temperature vs. density, characteristic of the flare decay phase (Reale, Serio, & Peres 1993). By considering a number of published values, Güdel et al. (2003) propose $\zeta = 0.5$–1, yielding $EMD \propto T^{3\pm1}$, which is consistent with the slope β we have derived above.

5.2.2. *Quasi-static corona hypothesis*

An alternative interpretation of the bulk of the EMD of AD Leo is in terms of quasi-static coronal loop structures, i.e., loops that evolve on time scales longer than the characteristic cooling time scale of the plasma (Serio et al. 1991)

$$\tau_{\rm c} \approx 120 \left(\frac{L}{10^9}\right) \left(\frac{T}{10^7}\right)^{1/2} \ \text{sec.} \qquad (1)$$

Since the pressure scale height at $T = 8\,$MK (EMD peak) is $H_{\rm p} \approx 1.6 \times 10^{10}\,$cm ($\sim 0.6 R_*$), loops shorter than this size are in isobaric state; this was the case for all the flaring structures studied by Favata et al. (2000a). In this hypothesis, the RTV scaling law

$$T_{\rm max} = 1.4 \times 10^3 (pL)^{1/3} \qquad (2)$$

together with the gas relation $p = 2 N_{\rm e} k_{\rm B} T$, yields

$$N_{\rm e}^2 L = 1.7 \times 10^{12} T_{\rm max}^4 L^{-1} \qquad (3)$$

which is approximately proportional to the emission measure per unit cross-sectional area of a single loop. By modeling the corona as an ensemble of loops all having the same characteristics and covering a fraction f of the visible hemisphere (hereafter, surface filling factor), we get a volume emission measure $EM = 2\pi R_*^2 f N_{\rm e}^2 L$, which scales as

$$EM \simeq 1.1 \times 10^{13} R_*^2 f T_{\rm max}^4 L^{-1} \qquad (4)$$

In a similar way, we can derive a scaling of the volume emission measure with the maximum temperature and the pressure, which reads

$$EM \simeq 3.0 \times 10^{22} R_*^2 f p T_{\rm max} \qquad (5)$$

Hence, through knowledge of the EMD and the plasma pressure (independently derived from spectroscopic diagnostics), we can in principle estimate the surface filling factor of the X-ray emitting coronal plasma.

The above coronal modeling, with the additional aspect of taking into account the detailed temperature and density profiles along the loops, was employed by Sciortino et al. (1999) to synthesize the total X-ray emission of AD Leo and to fit the available BeppoSAX spectra[5]. No estimate of the loop length or the plasma pressure was available at that time, and hence the best-fit solution was not unique, in the sense that the surface filling factor was constrained only by the requirement that the loops were isobaric ($L < H_{\rm p}$). This limitation does not affect the shape of the emission measure distribution but only its absolute normalization, and hence we have attempted a direct comparison of that coronal loop model solution with our current emission measure distribution. Fig. 9 shows such a comparison, having

[5]As mentioned above, Sciortino et al. (1999) performed their spectral analysis with a 2-loop model, i.e., consisting of two classes of coronal loops with different characteristics. Here and in the following we refer only to the dominant class, unless otherwise specified.

allowed for a down-scaling of the best-fit loop model solution by a factor ~ 2 to account for differences in the plasma metallicity and in some stellar parameters (distance and radius) with respect to the previous work. The agreement is striking, and confirms that our previous modeling was reasonable.

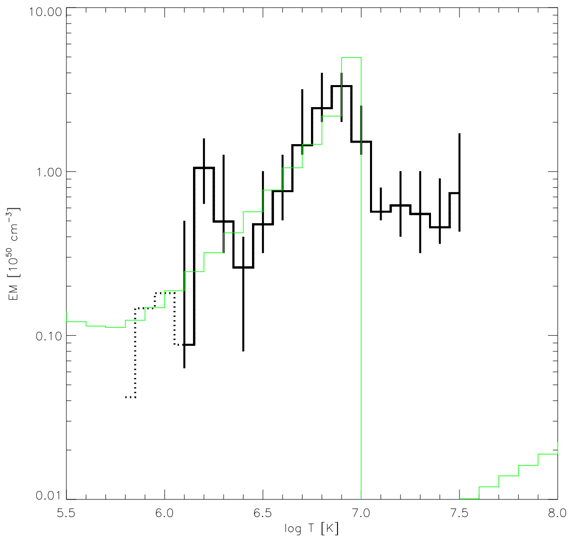

Fig. 9.— Comparison between the EMD derived from the *Chandra* data (heavy-line histogram) and the 2-loop model solution best-fitting the BeppoSAX spectra studied by Sciortino et al. (1999) (colored green in the electronic edition). The latter has been scaled to account for differences in the plasma metallicity and in the stellar parameters (distance and radius).

We are now in the position to employ the additional piece of information provided by our estimates of the plasma pressure. Since the emission measure distribution peaks at $\approx 10^7$ K, we can assume that the bulk of the coronal plasma is trapped in loops having this same value for $T_{\max}$, with a plasma pressure comparable to that suggested by the density-sensitive Fe XXI lines, i.e., $p \approx 5 \times 10^3$ dyn cm^{-2}. We have computed a loop model with the above parameters, yielding $L \sim 1.5 \times 10^8$ cm, and the related EMD: a good match with the reconstructed EMD of AD Leo can be obtained with a surface filling factor $f \sim 3 \times 10^{-4}$. This model suggests that, if static loops are invoked to explain the X-ray emission of AD Leo and plasma pressures of the order of 10^3 dyn cm^{-2} are assumed, very small ($L \lesssim 10^{-2} R_*$) coronal structures are required, covering a tiny fraction of the visible hemisphere ($f \ll 1\%$). For other parameter values, equation (5) tells us that the surface filling factor scales approximately as

$$f \approx 5 \times 10^{-4} \left(\frac{EM}{10^{50}}\right) \left(\frac{p}{10^3}\right)^{-1} \left(\frac{T}{10^7}\right)^{-1} \tag{6}$$

It is worth noting that the above model consists of structures much shorter than the flaring loops studied by Favata et al. (2000a), having $L \sim 0.15$–$0.5\,R_*$. If we assume, alternatively, that the corona is composed of a population of loops with $L = 0.3 R_*$ and $T_{\max} = 10^7$ K, we obtain a pressure $p \sim 45$ dyn cm^{-2} for the confined plasma and $f \sim 4\%$. This latter model appears difficult to reconcile with the actual pressure values.

On the other hand, the low plasma pressure ($p \sim 4$ dyn cm^{-2}) at $T \sim 2$ MK, probed with the O VII triplet, points toward the existence of an extensive population of cooler loops which may explain the low-temperature tail of the EMD of AD Leo. If we postulate that the secondary EMD peak at $T \sim 1.6 \times 10^6$ K is at the maximum temperature of these cool loops, application of equation (6) with

$EM = 10^{50}\,\mathrm{cm}^{-3}$ yields a very large filling factor, $f \sim 80\%$. Although not dominant in terms of total volume emission measure, the cool loop population possibly covers most of the visible hemisphere.

6. Summary and conclusions

We have performed a detailed analysis of the *Chandra*/LETG spectrum of the dMe flare star AD Leo, with the aim of deriving a distribution of the plasma emission measure vs. temperature, estimates of the plasma density at various temperatures by means of spectroscopic diagnostics, and measurements of the coronal abundances. We have employed these new results to test our knowledge of the corona of AD Leo, based on previous observations with more limited information content, and to improve our understanding of the thermal and spatial structuring of the coronal plasma in active red dwarfs with a "saturated" X-ray emission level.

The X-ray emission of AD Leo during the observation showed significant low-level variability, typical of such an active flare star. We have analyzed the X-ray spectrum accumulated during the entire observation, in order to derive information on the "average" properties of the corona in its characteristic unsteady, but quiescent state.

The X-ray spectrum of AD Leo, dominated by emission lines from O VII– VIII, Ne IX– X, Si XII– XIV, and Fe XVII– XXI ions, allowed us to reconstruct the emission measure distribution (EMD) in the temperature range $10^{5.8}$–$10^{7.5}$ K and to estimate the abundance ratios of the most common α elements with respect to iron.

A crucial aspect of our analysis concerns the selection of the line measurements to be employed for the reconstruction of the EMD. We discarded the Ne X Lyα line because it appears a factor ~ 2 less intense than predicted by the EMD, with respect to the other Ne lines of the Lyman series. This effect could be due to resonant line absorption or to processes of population of the atomic levels not yet taken into account properly by the available plasma emissivity codes (see the case of the O VIII Lyα/Lyβ ratio presented by Smith et al. 2001).

The EMD peaks at $T \approx 8$ MK and can be approximated with a power law with slope 2 ± 1, in the temperature range 2.5–8 MK; a secondary maximum occurs at 2 MK, and a substantial fraction of the emission measure is present also at temperatures beyond the peak, up to $T \approx 30$ MK. The shape of the EMD is in good agreement with that derived from previous analysis of EUVE spectra: this result strengthens our confidence in the robustness of a line-based approach for the emission measure analysis and confirms the "stability" of the thermal configuration of the corona of AD Leo on time scales of several years. In particular, the bulk of the EMD appears to be continually present, unrelated to any evident flaring phase. Flares with medium or large amplitudes likely have significant effects only on the hot tail of the EMD.

While the emission measure peak occurs at approximately the same temperature as in the EMDs of previously studied active binaries or single G-K dwarfs and Hertzsprung gap giants, the shape of the EMD is significantly shallower than that generally obtained in these other cases. With only this single example, we cannot establish whether this feature is characteristic of just dMe stars, or of stars with medium-low X-ray luminosity ($L_{\rm x} \approx 10^{28}\,{\rm erg~s^{-1}}$). At variance with the case of other high-luminosity active stars, the slope of the EMD is in agreement (within uncertainties) with that predicted by models of coronal loops shorter than the pressure scale height, with constant cross-section and uniform heating. In particular, the present EMD is well matched by the static loop model employed by Sciortino et al. (1999) to fit the BeppoSAX spectra of AD Leo. On the other hand, the slope is also in agreement with that predicted by the model of a corona entirely heated by continuously flaring loops, developed by Güdel et al. (2003).

In order to test the quasi-static corona model against the continuous flaring model, we have considered estimates of the plasma pressure at various temperatures, obtained by means of density-sensitive line ratios from He-like triplets and Fe XXI lines. The computed pressures appear to increase with increasing temperature, a result which we interpret as evidence of different classes of coronal structures that are not in pressure equilibrium. In particular, while the O VII triplet yields pressures of 0.5–10 dyn cm^{-2} at 2 MK, the Fe XXI lines suggest $p \approx 10^3$–10^4 dyn cm^{-2}. This result also has relevance to the interpretation of the EMD in terms of quasi-static loops. For loops of constant cross-section, $EM(T) \propto T^{3/2}$; as we noted earlier, this power law is similar to that observed. However, a loop model matching the hot part of the EMD and containing gas at the high pressure found at these temperatures also requires the same high pressure at lower temperatures. The disparity between the different pressure estimates at 2 MK and 10 MK requires that the hot high-pressure loops yield a negligible contribution to the plasma emission measure at 2 MK; in turn, this result implies that the EMD of the hot loops should be sufficiently steep, possibly steeper than constant cross-section uniformly-heated models allow.

If we assume that the bulk of the X-ray emission comes from static loops with high-pressure plasma, the EMD requires very small loop structures ($L < 10^{-2} R_*$) whose footpoints cover a tiny fraction ($f \ll 1\%$) of the visible hemisphere; these model loops are significantly shorter than the loops undergoing flaring events, studied by Favata et al. (2000a), which have $L \approx 10^{-1} R_*$. Following this hypothesis leads to a scenario in which the corona consists of a steady population of short, high-pressure loops, while the large flares are due to another population of longer loops, possibly those suggested by the hot tail of the EMD.

The small surface filling factor of the main loop population can be easily reconciled with the lack of any large-amplitude variability of the X-ray emission: if the loops are uniformly distributed over the stellar surface, we do not expect any clear rotational modulation of the coronal emission, and on the other hand, in case of flares, the small size of these loops ($L \sim 10^8$ cm) implies very short thermodynamic cooling times ($\tau_{\rm c}$ of the order of 10 sec according to equation 1), i.e. the X-ray emission from these loops is so rapidly variable that no evident flare can be discerned in the light curve. This argument may also explain why the loops associated with *visible* flares are preferentially found to be relatively larger.

Finally, the derived coronal abundances, relative to solar values, tend to increase with the First Ionization Potential, as in other active stars. A puzzling result is that the absolute iron abundance in the corona of AD Leo derived here, based on the observed line to continuum ratio, suggests a nearly solar metallicity of the plasma, contrary to previous findings from low resolution X-ray spectra that indicated $[Fe/H] \sim -0.6$. Notable results for individual elements include enhancements relative to Fe of S by a factor of about 7, of Ne by a factor of 5, and of Si by a factor of 2.5.

AM, SS, GM, and GP acknowledge partial support from Ministero dell'Universitá e della Ricerca Scientifica. VK and JJD acknowledge support from NASA contracts NAS8-39073 and NAS8-03060 to the *Chandra* X-ray Center; JJD also thanks the NASA AISRP for providing financial assistance for the development of the PINTofALE package under NASA grant NAG5-9322. FRH acknowledges partial support from NASA contracts NAS8-38248 and NAS8-01130.

A. Data analysis and emission line spectroscopy issues

In this appendix we describe some details of our spectral analysis of the X-ray emission of AD Leo, its reliability and robustness and the limitations of our line-based approach.

A.1. Line identification and fitting

The line identification list in Table 3 is not intended to be complete. We have instead focussed our attention on significant features that could be useful in the emission measure analysis. In the 36–66 Å region – where most of the 3rd order spectrum falls – several features have escaped identification, as have with a few more at long wavelengths ($\lambda > 80$ Å) where the spectrum is more noisy.

The most intense lines are those from the (unresolved) O VIII Lyα doublet (λ18.967, 18.972), the Ne X Lyα doublet +Fe XVII blend at 12.12 Å, the Ne IX+Fe XIX blend at 13.45 Å, the Fe XVII line at 15.02 Å and the resonance line of the O VII triplet at 20.60 Å.

Among the identified iron lines, note in particular the several Fe XXII–Fe XXIV lines in the region between 10.6 Å and 11.8 Å, which also includes many weak Fe XVII–Fe XIX lines not listed in the CHIANTI database but present in the Astrophysical Plasma Emission Database (APED).

At long wavelengths (80 – 140 Å) we have identified several Ne VIII and Fe XVIII–XXIII lines observed in previous EUVE spectra: Fig. 10 shows a comparison between the present *Chandra*/LETG spectrum and the exposure-weighted sum of the nine EUVE spectra taken between 1993 and 2000 (Sanz Forcada & Micela 2002). The *Chandra* spectrum has been smoothed with a bin size of 0.4 Å to match the FWHM resolution of the short-wavelength (SW) EUVE spectrometer, and both spectra are in calibrated absolute flux units (having taken into account the instrument effective area). There is a remarkable overall agreement between the two data sets, which secures most of the identifications we have made in the *Chandra* spectrum. In particular, we note the detection of the density-sensitive lines from Fe XX at λ 110.63 Å, Fe XXI at λ 121.21 Å, and Fe XXII at λ 114.41 Å, which hint at the presence of high-density plasma

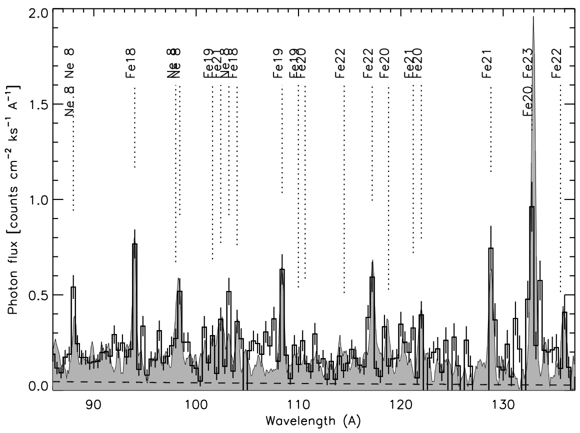

Fig. 10.— Long wavelength region of the AD Leo LETG spectrum (thick line histogram with error bars), compared with the total EUVE spectrum (thin line, shaded) obtained as the sum of nine observations. The *Chandra* spectrum has been rebinned to match the EUVE spectral resolution (FWHM $\sim$ 0.4 Å), and both spectra were converted to absolute photon flux units (i.e., divided by the respective instrument effective areas).

($N_e \gtrsim 5 \times 10^{11}$ cm^{-3}) in the corona of AD Leo.

Central wavelengths and integrated line fluxes have been determined by line fitting using Moffat profiles, i.e., a modified Lorentzian functional form,

$$L_\beta(x) = \frac{A}{[1 + ((x - x_0)/\sigma)^2]^\beta} \qquad \text{(A1)}$$

plus a piece-wise constant base level, adjusted to match the source continuum predicted by the final emission measure distribution vs. temperature. The exponent $\beta = 1.8$ and $\sigma = 0.035$ in the above equation were determined by fitting the most intense and isolated features in the spectrum (Ne X+Fe XVII λ 12.12 Å, Fe XVII λ 16.78 Å, O VIII λ 18.97 Å, O VII λ 21.60 Å, C VI λ 33.73 Å), and then keeping these parameters fixed for all the other lines. Line fitting was performed using multiple components where required by recognized line blends, and errors at the 68% confidence level have been also evaluated for each single interesting parameter ($\Delta\chi^2 = 1$). Special attention was paid in fitting the He-like triplets from the Si XIII and Ne IX ions, and the better resolved triplet of the O VII ion. Results of these fits are shown in Fig. 11. The Mg XI triplet has been also detected, but it is relatively weaker and more noisy than the others, and line fluxes determined therefrom have quite large uncertainties.

Comparison between observed and model wavelengths, i.e., between the fitted line center values and the nominal values from the CHIANTI line identification list, are shown in Fig. 12: the agreement is generally good, within 0.02 Å, except for a positive shift by up to 0.05 Å for few lines

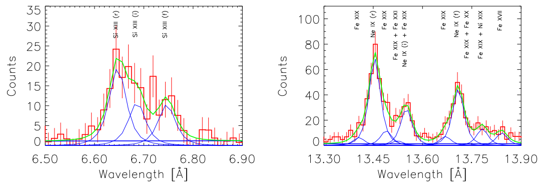

Fig. 11.— Si XIII and Ne IX He-like triplets. The two panels show the components used to de-blend the line complexes, and the continuum level (in the electronic edition, the individual line components and the continuum are colored blue, while the total model spectrum is green). Note the mixture of Ne and Fe lines in the wavelength range of the Ne IX triplet.

at wavelength > 40 Å, likely due to residual uncertainties in the wavelength calibration.

A.2. Emission measure distribution (EMD) and element abundances

Emission measure analysis and abundance determination were performed in several steps. First, following Pottasch (1964), we constructed inverse emissivity curves for all the detected iron lines, with the aim to select a subset of them complying with the criterion that the inverse emissivity curves for lines of the same ion should agree. Single discrepant lines were discarded, and we have verified that in most cases they are affected by problems like heavy blending with other known lines, anomalous profiles, low S/N ratio, or dependence on the plasma density. Especially problematic are the Fe XVIII and Fe XIX lines: among the 14 Fe XVIII lines with more than 20 integrated counts, only

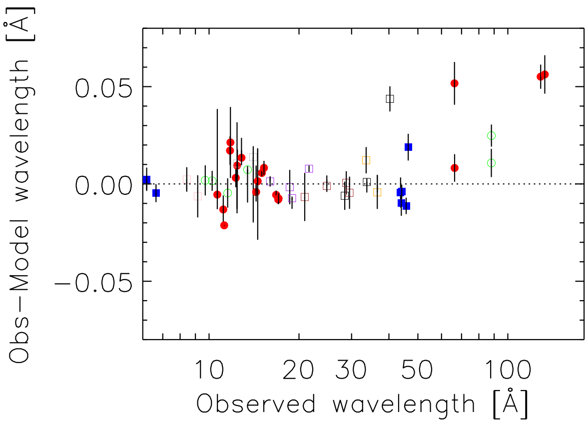

Fig. 12.— Differences between the measured (best-fit) wavelength (with associated 1σ error) and the nominal value (based on the CHIANTI identifications), plotted vs. the measured wavelength, for the strongest lines in the spectrum (filled circles:Fe; open circles: Ne; filled squares: Si; open squares: others; in the electronic edition, different elements are colored as in Fig. 3). The agreement is within 0.03 Å in all cases except a few lines at wavelengths $\lambda > 40$ Å, likely due to residual uncertainties in the wavelength scale.

two ($\lambda\lambda 14.37, 14.55$ Å) have been included in the final selection because most of the others have measured fluxes that differ from those predicted by more than a factor 2 (i.e., the observed line ratios do not agree – in most cases – with those based on the CHIANTI emissivities and the final EMD). Furthermore, none of the Fe XIX lines was selected because they are either severely blended or are too weak for reliable line fitting.

We then performed a similar selection for the lines of the other elements, one at a time, in the following order: Si, Mg, Ne, O, N, C, and finally S and Ni. This sequence is such that the line emissivities always have some temperature range in common with those of the preceding group, and hence the relative abundance of each element can be guessed by forcing the overlap of its inverse emissivity curves with those of the other elements in that range. With the above procedure we selected about half of the lines in our list, thereby obtaining a first, rough estimation of the element abundances with respect to Fe.

The next step was to apply the Markov-Chain Monte Carlo (MCMC) method of Kashyap & Drake (1998) to derive consistently the EMD, the element abundances, and the associated uncertainties. This method essentially performs a search in the parameter space (comprising a set of emission measure values, defined over a preselected temperature grid, and a set of element abundances depending on the chosen emission lines) while attempting to maximize the probability that the observed and predicted line fluxes are drawn from the same parent population. An important characteristic of this method is that formal statistical uncertainties on individual free parameters can be obtained from the distribution of values in the sampled region of the parameter space near the final maximum-probability solution. In practice, uncertainties are available only for a subset of the emission measure values among those in the EMD, depending on the availability of observed lines with sensitivity adequate to each selected temperature.

A critical feature of this method is the choice of the temperature range where the EMD is reconstructed: it should be large enough to cover the tails of the emissivity functions of the selected lines with the lowest and the highest formation temperature, because significant contributions to the integrated line flux may come from substantial amount of plasma located relatively far from the emissivity peak. On the other hand, since the emission measure values at the extremes of the temperature range tend to be determined by fewer and weaker lines than the values near the peak of the EMD, the uncertainties on the EMD tails become larger and larger for increasing width of the explored temperature range. We have performed two different tests to test the reliability of the EMD tails: a careful comparison of the model spectrum, based on the full EMD, with the observed spectrum at relatively long wavelengths (20–100 Å) can reveal whether or not the emission measure at the low-temperature end is overestimated, because in that case several low-ionization lines (e.g. Si X, Si XI) are predicted but not observed. Instead, the EMD high-temperature tail affects the *shape* of the continuum in the critical short-wavelength range 5–9 Å, and comparison with the observed spectrum in this range has allowed us to test the reconstructed EMD. Based on the above two tests, we have chosen an optimal temperature range for the emission measure analysis ($\log T \sim 5.8$–7.5 K). The same tests also suggest that the uncertainties on the emission measure near the extremes of the temperature range are likely larger than the formal values determined in each single run of the MCMC procedure.

A second delicate aspect of the analysis is the line selection, and in particular the possible bias introduced by the strongest resonance lines, namely the Lyα lines from hydrogenic ions and the iron lines which form near the peak of the EMD (Fe XVII in the case of AD Leo). As a matter of fact, the accuracy of the atomic databases and of the model EMD we derive under the usual (wide) set of assumptions (optically-thin emission from a plasma in ionization equilibrium with uniform abundances) is such that we are currently able to predict most of the observed emission lines, but not better than to within a factor 2. This systematic uncertainty is in many cases much larger than the statistical uncertainty on the measurements, especially for the strong lines mentioned above, with the consequence that the emission measure analysis can be adversely influenced by the attempt to match the observed flux of these lines. The case of the Ne X Lyα line + Fe XVII is revealing: this is the strongest spectral feature among those dominated by Ne lines, and – when it is included in the selected line list – the MCMC procedure yields an EMD and Ne/Fe abundance ratio that predict the observed flux of this line almost perfectly. With this choice, however, all other Ne lines are systematically over-predicted, with the isolated Ne X Lyβ line at 10.24 Å over-predicted by more than a factor 2. With the Lyα line instead excluded, the new EMD and Ne/Fe value provide a fair prediction of all the Ne lines (Fig. 4), but the observed flux of the Lyα line is lower than predicted by a factor $\lesssim 2$. Possible reasons for this behavior were discussed in Sect. 4.

Finally, we discuss the issue of missing lines in the CHIANTI database. As discussed by Argiroffi et al. (2003) and by Scelsi et al. (2003), the CHIANTI database is currently less complete than the APED database, especially in the wavelength region 10–12 Å where hundreds of weak lines from Fe XVII– XIX fall. This spectral region also includes the most relevant L-shell lines from Fe XXII– XXIV, which are crucial to constrain the high-temperature tail of the EMD. Most of these lines are blended with iron lines of lower ionization stages, whose contributions need to be taken into account. Due to the incompleteness of the CHIANTI database, we have adopted the following approach: the EMD was initially reconstructed including only lines in the CHIANTI database; then, we synthesized the predicted model spectrum using the APED V1.3 database, and evaluated any possible (previously missed) contribution to the relevant Fe XXII– XXIV lines. The measured line fluxes of these latter lines were then multiplied by a correction factor (< 1, essentially a blending fraction), and the emission measure analysis was iterated until convergence was achieved. The affected lines with their estimated blending fraction, based on APED, are as follows: Fe XXIV $\lambda 10.66$ (60% contamination), $\lambda 11.17$ (70%), $\lambda 11.26$ (90%). A similar correction was also applied to the Ne IX line at 11.55 Å (30% contamination). We stress that, if the above correction is not applied, the overestimated strength of the Fe XXII– XXIV lines yields an EMD with a more pronounced high-temperature tail. Most of the high-ionization Fe lines remain under-predicted by the EMD model, however, because the EMD at $T \gtrsim 10^7$ K cannot grow arbitrarily, due to the constraints provided by other lines from Fe XXI, Fe XXIII, Mg XII, and Si XIV ions (Fig. 3).

A.3. Metallicity

We have identified two wavelength regions where a comparison between the observed spectrum and the predicted continuum emission level is especially useful for determining the plasma metallicity: the range 6–9 Å, where the cutoff of the bremsstrahlung emission from the hottest plasma ($T \sim 2 \times 10^7$ K) occurs, and the region long-ward of the C K-edge ($\lambda \gtrsim 44$ Å), where the jump in the instrument effective area makes the continuum visible again. A close inspection of Fig. 5 reveals that, in both regions, a reasonably good agreement can be reached only for Fe/H ratios ≥ 0.8 the solar value. The relatively low continuum level, due to this metallicity value, makes it difficult to constrain the iron abundance: in fact, an increase of Fe/H by a factor 2 (i.e., from $Fe/H = 0.8$ to 1.6 times solar) implies a small change in the predicted continuum level, comparable to the uncertainty in the observed count rate due to Poisson statistics. For this reason we have conservatively deduced for AD Leo a metallicity comprised in the range 0.8 – 1.6 times the solar photospheric value ($\log A_{\rm Fe} = 7.51 \pm 0.05$, where $\log A_{\rm H} = 12$). Such a metallicity determination implies that a large fraction of the apparent continuum between 5 and 15 Å is actually due to emission lines.

A.4. Density and temperature diagnostics

The O VII He-like triplet is the only well-resolved triplet in *Chandra*/LETG spectra. Nonetheless, two issues are relevant for a correct estimation of the plasma (effective) density and temperature: the placement of the continuum level, which affects the measurement of the line fluxes, as demonstrated by Brickhouse et al. (2002), and the proper treatment of transitions from high-n states (Porquet, Mewe & Dubau 2001; Smith et al. 2002). The continuum we have used is that predicted by the EMD, and hence it should not suffer of misplacement problems due to unresolved weak lines in the relevant wavelength range. In order to check for possible deficiencies in the CHIANTI database, we compared our estimated density and temperature with those predicted by the model of Porquet, Mewe & Dubau (2001) for the same measured O VII line ratios and found complete agreement between them. Our result is also consistent with that obtained by Ness et al. (2002), based on the latter model.

More problematic is the proper measurement of the line fluxes in the Ne IX triplet, because of the heavy blending with Fe XIX lines, and to a lesser extent also Fe XX– XXI lines. Ness et al. (2003) have recently performed a detailed analysis of the Ne IX triplet spectral region in *Chandra* and XMM-Newton spectra of Capella, and concluded that the Astrophysical Plasma Emission Code (APEC) models are sufficiently accurate and complete that all significant observed lines in this region can be reasonably identified in the *Chandra*/HEG; they also argue that spectra obtained by LETGS are inadequate to derive reliable results independently. In order to measure the line fluxes in our AD Leo spectrum we have performed a multi-component line fitting by taking into account most of the spectral features listed by Ness et al. (2003). Moreover, for the resonance, intercombination, and forbidden Ne IX lines we have evaluated the (density-dependent) contamination due to unresolved iron lines, as predicted by the model spectrum and both the CHIANTI and APED databases. In Table 6 we report the blending fraction in the low-density limit for both atomic databases, and at the estimated plasma density in the corona of AD Leo for CHIANTI only. While the contamination of the resonance line is the same in all cases, the blending fraction for the intercombination line decreases for increasing density (because only the Ne contribution is density-dependent), and the opposite occurs for the forbidden line, as expected. Rather surprising is the finding that in the low-density limit, the CHIANTI database predicts a larger blending fraction than APED.

In order to compute the relevant density- and temperature-sensitive ratios we subsequently corrected the measured line fluxes, in a self-consistent way, for the blending fraction computed according to CHIANTI. Both the temperature and density determinations (Table 5) are in agreement with the alternative estimates based on the Porquet, Mewe & Dubau (2001) model. However, at variance with Ness et al. (2002), our analysis suggests a plasma density significantly above the low-density limit: in fact, Fig. 13 shows excess emission at the location of the intercombination line with respect to the low-density predictions based either on CHIANTI or APED. On the other hand, both model spectra show locations of the emission peaks (corresponding to the resonance and forbidden lines) that are shifted by one bin (0.0125 Å) with respect to the data, which we interpret as evidence of uncertainties in the atomic databases related to the wavelength of the emission lines or to the relative emissivities, or both.

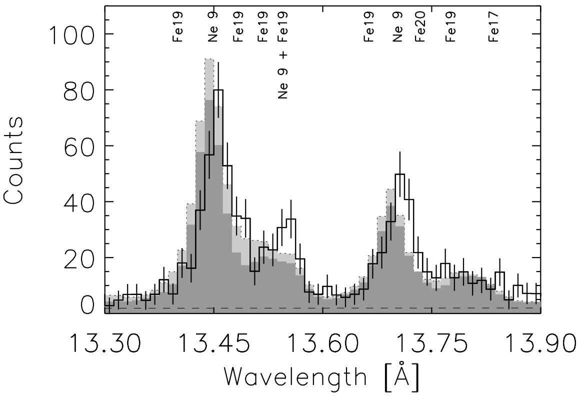

Fig. 13.— The Ne IX triplet spectral region with model predictions in the low-density limit based on the reconstructed emission measure distribution and the CHIANTI (dark shade) or APED (dot-bounded light shade) line emissivities. The excess emission observed at $\lambda \sim 13.5$ Å is suggestive of a high-density effect.

For the Si XIII triplet we followed a similar procedure. In this case, a minor contamination (blending fractions < 4%) to the intercombination and forbidden lines is due mainly to Si XII satellite lines. The CHIANTI density and temperature estimates are again compatible, within uncertainties, with those based on the Porquet, Mewe & Dubau (2001) model. However, some difficulty with the atomic models arises from the finding that the Ne IX and Si XIII temperature-sensitive ratios, R_{T}, are quite high, yielding estimates of the plasma temperature that are significantly lower than the average values weighted by the line emissivity function and by the EMD. This puzzling result was recently noted in other contexts (Argiroffi et al. 2003; Ness et al. 2003), but a clear explanation is not yet available.

Finally, we looked for density-sensitive Fe XX– XXII lines in the AD Leo spectrum. These lines provide independent estimates of the plasma density at temperatures ($T \sim 10^7$ K) similar to those at which the Si XIII triplet forms, and they have been commonly employed in studies of EUVE spectra (Sanz Forcada & Micela 2002). In the AD Leo spectrum we tentatively identified the lines Fe XX λ110.63, Fe XXI λ121.20, and Fe XXII λ114.41, which become clearly visible only in high-density plasmas ($N_{\mathrm{e}} \gtrsim 10^{11}$–$10^{12}\,\mathrm{cm}^{-3}$). These lines have only a few tens of integrated counts, and the relevant spectroscopic diagnostics (provided by the line ratios 110.63/121.84, 121.2/128.75, 114.41/117.18) yield density estimates affected by large error bars. The most precise result is that derived from the Fe XXI line ratio and reported in Table 5, suggesting a plasma density $N_{\mathrm{e}} \sim 10^{12}\,\mathrm{cm}^{-3}$.

REFERENCES

Ambruster, C. W., Sciortino, S., & Golub, L. 1987, ApJS, 65, 273

Argiroffi, C., Maggio, P., & Peres, G. 2003, A&A, 404, 1033

Audard, M., Güdel, M., Drake, J. J., & Kashyap, V.L. 2000, ApJ, 541, 396

Ayres, T. R., Simon, T., Stern, R. A., Drake, S. A., Wood, B. E., & Brown, A. 1998, ApJ, 496, 428

Brickhouse, N. 2002, in ASP Conf. Proc. 277, Stellar Coronae in the *Chandra* and XMM-Newton Era, ed. F. Favata and J. Drake, 13

Table 6
Blending fractions[a] for the Ne IX triplet

	APED	CHIANTI	
Line	Low-density	Low-density	5×10^{11} cm^{-3} [b]
r	6%	6%	6%
i	22%	31%	22%
f	2%	3%	4%

[a]Fraction of flux from contaminating Fe lines in a range of about 0.02 Å centered on the Ne line.

[b]Estimated electron density from corrected f/i ratio.

Brinkman, A. C. et al. 2001, A&A, 365, L324

Collura, A., Pasquini, L., & Schmitt, J. H. M. M. 1988, A&A, 205, 197

Cully, S., Fisher G., Hawley S. L., & Simon T. 1997, ApJ, 491, 910

Dere, K. P., Landi, E., Young, P. R., & Del Zanna, G. 2001, ApJS, 134, 331

Drake, J. J. 2002, in ASP Conf. Ser. 277, Stellar Coronae in the Chandra and XMM-NEWTON Era, ed. F. Favata & J. J. Drake, ASP:San Francisco, 75

Drake, J. J. 2003, Adv. Space Res., 32, 945

Drake, J. J., Peres, G., Orlando, S., Laming, J. M., & Maggio, A. 2000, ApJ, 545, 1074

Favata, F., Micela, G., & Reale, F. 2000a, A&A, 354, 1021

Favata, F., Reale, F., Micela, G., Sciortino, S., Maggio, A., & Matsumoto, H. 2000b, A&A, 353, 987

Feldman, U., & Laming, J. M. 2000, Phys. Scr, 61, 222

Giampapa, M. S., Rosner, R., Kashyap, V., Fleming, T. A., & Schmitt, J. H. M. M. 1996, ApJ, 463, 707

Grevesse, N., Noels, A., & Sauval, A. J. 1992, in ESA SP-348, Coronal Streamers, Coronal Loops, and Coronal Wind Composition, 305

Griffiths, N. W., & Jordan, C. 1998, ApJ, 497, 883

Güdel, M., Audard, M., Kashyap, V. L., Drake, J. J., & Guinan, E. F. 2003, ApJ, 582, 423

Güdel, M., Audard, M., Reale, F., Skinner,

S. L., & Linsky, J. L. 2004, A&A, 416, 713

Jenkins, L. F. 1952, Catalogue of Trigonometric Parallaxes (New Haven: Yale Univ. Obs.)

Jones, H. R. A., Longmore, A. J., Allard F., & Hauschildt, P. H. 1996, MNRAS, 280, 77

Kashyap, V., & Drake, J. J. 1998, ApJ, 503, 450

Kashyap, V., & Drake, J. J. 2000, BASI 28, 475

Kashyap, V. L., Drake, J. J., Güdel, M., & Audard, M. 2002, ApJ, 580, 1118

Naftilan, S. A., Sandmann, W. S., & Pettersen, B. R. 1992, PASP, 104, 1045

Ness, J.-U., Brickhouse, N., Drake, J. J., & Huenemoerder, D. P. 2003, ApJ, 598, 1277

Ness, J.-U., Schmitt, J. H. M. M., Burwitz, V., Mewe, R., Raassen, A. J. J., van der Meer, R. L. J., Predehl, P., & Brinkman, A. C. 2002, A&A, 394, 911

Maggio, A., Drake, J. J., Harnden, F. R., Jr., Kashyap, V. L., Micela, G., Murray, S. S., Peres, G., & Sciortino, S. 2001, in ASP Conf. Ser. 234, X-ray Astronomy 2000, ed. R. Giacconi, L. Stella, S. Serio, on CD-ROM

Maggio, A., Drake, J. J., Jr., Kashyap, V. L., Micela, G., Peres, G., Sciortino, S., Harnden, F. R., Jr., & Murray, S. S. 2002, in ASP Conf. Proc. 277, Stellar Coronae in the *Chandra* and XMM-NEWTON Era, ed. F. Favata, J. J. Drake, 57

Maggio, A., & Peres, G. 1996, A&A, 306, 563

Mazzotta, P., Mazzitelli, G., Colafrancesco, S., & Vittorio, N. 1998, A&AS, 133, 403

Peres, G., Orlando, S., Reale, F., Rosner, R., & Hudson, H. 2000, ApJ, 528, 537

Pizzolato, N., Maggio, A., Micela, G., Sciortino, S., & Ventura, P. 2003, A&A, 397, 147

Porquet, D., Mewe, R., & Dubau, J. 2001, A&A, 376, 1113

Pottasch, S. R. 1964, Space Sci. Rev. 3, 816

Reale, F., & Micela, G. 1998, A&A, 334, 1028

Reale, F., Peres, G., & Orlando, S. 2001, ApJ, 557, 906

Reale, F., Serio, S., & Peres, G. 1993, A&A272, 486

Rosner, R., Tucker, W. H., & Vaiana, G. S. 1978, ApJ, 220, 643

Sanz Forcada, J., Brickhouse, N. S., & Dupree, A. K. 2003, ApJS, 145, 147

Sanz Forcada, J., Favata, F., & Micela, G. 2004, A&A, in press

Sanz Forcada, J., Maggio, A., & Micela, G. 2003, A&A, 408, 1087

Sanz Forcada, J., & Micela, G. 2002, A&A, 394, 653

Scelsi, L., Maggio, A., Peres, G., & Gondoin, Ph. 2004, A&A, 413, 643

Schmitt, J. H. M. M., & Favata, F. 1999, Nature, 401, 44

Sciortino, S., Maggio, A., Favata, F., & Orlando, S. 1999, A&A, 342, 502

Serio, S., Peres, G., Vaiana, G. S., Golub, L., & Rosner, R. 1981, ApJ, 243, 288

Serio, S., Reale, F., Jakimiec, J., Sylvester, B., & Sylvester, J. 1991, A&A, 241, 197

Smith, R. K., Brickhouse, N. S., Liedahl, D. A., & Raymond, J. C. 2001, ApJ, 556, 91

Testa, P., Drake, J. J., Peres, G., & DeLuca, E. E. 2004, ApJ, submitted

van den Besselaar, E. J. M., Raassen A. J. J., Mewe, R., van den Meer, R. L. J., Güdel, M., Audard M. 2003, A&A, 411, 587

Weisskopf, M. C., Brinkman, B., Canizares, C., Garmire, G., Murray, S., & Van Speybroeck, L. P. 2002, PASP, 114, 1

This 2-column preprint was prepared with the AAS LaTeX macros v5.0.